Journal of Materials Chemistry B

Rhodamine-Derived Ratiometric Fluorescent Probes for High-Sensitivity Detection and Real-Time Imaging of Mitochondrial pH and Viscosity in HeLa Cells and Drosophila Melanogaster

Journal:	*Journal of Materials Chemistry B*
Manuscript ID	TB-ART-03-2025-000747.R2
Article Type:	Paper
Date Submitted by the Author:	27-May-2025

Complete List of Authors:	Pandey, Subash; Michigan Technological University, Department of Chemistry Arachchige, Dilka; Michigan Technological University, Department of Chemistry Schwandt, Ronald J.; Michigan Technological University, Department of Chemistry Dwivedi, Sushil; Michigan Technological University, Department of Chemistry Kathuria, Ishana; Michigan Technological University, Department of Chemistry Liu, Haiying; Michigan Technolgical University, Department of Chemistry Luck, Rudy; Michigan Technological University, Department of Chemistry

Rhodamine-Derived Ratiometric Fluorescent Probes for High-Sensitivity Detection and Real-Time Imaging of Mitochondrial pH and Viscosity in HeLa Cells and *Drosophila Melanogaster*

Subash Pandey, Dilka Liyana Arachchige, Ronald J. Schwandt, Sushil K. Dwivedi, Ishana Kathuria, Haiying Liu, Rudy L. Luck*

Department of Chemistry, Michigan Technological University, Houghton, MI 49931.
*Corresponding author.
*E-mail: rluck@mtu.edu

Highlights

- Two ratiometric probes (**A** and **B**), incorporating FRET/TBET mechanisms and spirolactam-switched rhodamine acceptors, enable sensitive, real-time tracking of mitochondrial pH with enhanced specificity, particularly under oxidative stress, hypoxia, and mitophagy.
- Coumarin and nitrobenzofurazan fluorophores are employed as energy donors via FRET or TBET mechanisms activated by a spirolactam ring switch attached to a near-infrared rhodamine acceptor.
- Probes exhibit high sensitivity to both acidic and alkaline pH conditions, enabling the visualization of transient pH shifts within mitochondria and lysosomes.
- Probe **A** can be used to track the viscosity changes in cells at a fixed pH value.

Abstract

The spirolactam on/off switch attached to rhodamine dye is known to be a highly selective and sensitive fluorescent probe, yet few studies have explored extending the π-conjugation system within its skeleton for pH detection in live cells. An extended π-conjugated rhodamine section should enable ratiometric pH detection in the near-infrared region. In this study, we synthesized probes **A** and **B** by coupling a rhodamine derivative with 7-nitrobenzofurazan and 7-(diethylamino)-2-oxo-3,8a-dihydro-2H-chromene-3-carbaldehyde sections, respectively. Probe **A** exhibits absorbance via a Förster resonance energy transfer (FRET) mechanism. Under excitation at 370 nm, the conjugated 7-nitrobenzofurazan in probe **A** exhibits fluorescence at 465 nm in the ring-closed state, while fluorescence at 660 nm appears in the ring-open state due to increased conjugation in the rhodamine moiety. Excitation of probe **B** at 325 nm resulted in reduced emission

around 350 nm and a significantly enhanced response at 525 nm. Probe **A** was evaluated for mitochondrial pH detection through ratiometric fluorescence emission measurements. Additional tests in living HeLa cells, including responses to stimuli such as carbonyl cyanide-4(trifluoromethoxy)phenylhydrazone (FCCP), hydrogen peroxide (H_2O_2), N-acetyl cysteine (NAC), mitophagy induced by nutrient deprivation, and hypoxia triggered by cobalt chloride ($CoCl_2$) treatment, as well as pH changes in fruit fly larvae, further validated its applicability for ratiometric measurement of mitochondrial pH variations. Probe **A**'s emission was dependent on the pH level under basic conditions, but under acidic conditions, the change in conformation upon ring opening resulted in the emission also being affected by viscosity.

Introduction

Intracellular pH is a critical factor regulating key biological processes, including ion transport, cell signaling, energy metabolism, division, migration, apoptosis, and protein folding.[1–7] The pH varies across different cellular regions, with each organelle maintaining distinct pH levels suited to its functions.[8,9] For instance, mitochondria exhibit an alkaline environment (pH ~8.0) due to proton extrusion through the electron transport chain.[10,11] This alkaline pH is essential for mitochondrial function, including ATP production, calcium homeostasis, reactive oxygen species (ROS) signaling, and regulation of cell aging and death.[12–15] Minor pH fluctuations can significantly impact mitochondrial activity, particularly under stress conditions such as hypoxia, oxidative stress, or starvation, where acidification often occurs.[16] For example, during mitochondria-associated autophagy (mitophagy),[17,18] mitochondrial pH may decrease from 8.0 to 4.5, a disruption linked to neurodegenerative diseases, cardiomyopathy, cancer, and metabolic disorders.[19] Thus the importance of acidic pH-activatable fluorescent probes for live-cell organelle targeted imaging.[20–22] Similarly, oxidative stress-induced ROS accumulation triggers pH changes, reflecting mitochondrial dysfunction or adaptive responses. Monitoring these dynamic pH shifts is crucial for understanding mitochondrial physiology and its role in health and disease. Conventional fluorescence intensity-based probes are widely used for pH monitoring but suffer from limitations such as photobleaching, probe concentration dependence, and environmental variability. In contrast, ratiometric fluorescence probes offer superior reliability through self-calibration, reduced background interference, and enhanced accuracy, making them ideal for studying complex cellular systems.

Recent advances[23,24] include biocompatible pH-sensitive fluorescent probes, such as those developed by Lee et al.,[20] featuring a piperazine-based naphthalimide for real-time monitoring of mitochondrial acidification during mitophagy, and Bai et al.'s reversible rhodamine-based ratiometric probe for dual-emission imaging of mitochondrial pH. Rhodamine, with its spirocyclic structure,[25,26] has gained attention for its unique fluorescence activation under acidic conditions,[27] high optical performance, targeted tracking of organelles,[28,29] and low detection limits.[30,31] However, conventional rhodamine-based probes often emit in the visible spectrum, increasing the risk of photodamage.[32] Fluorescence resonance energy transfer (FRET)-based ratiometric fluorescent probes offer distinct advantages, including self-calibration and high sensitivity.[33,34] Unlike intensity-based fluorescent probes, ratiometric probes can eliminate systematic errors caused by instrument calibration, sample heterogeneity, uneven dye distribution, and compartmental localization.[35,36]

In this study, we developed two novel ratiometric fluorescent probes (probes **A** and **B**, Scheme 1) to monitor mitochondrial pH dynamics under oxidative stress, hypoxia, and mitophagy. These probes integrate coumarin and nitrobenzofurazan fluorophores as Förster resonance energy transfer (FRET) or through-bond energy transfer (TBET) acceptors with a near-infrared rhodamine derived donor. The nitrobenzofurazan donor facilitates partial opening of the rhodamine spirolactam ring under mildly alkaline conditions, enabling dual-emission fluorescence for precise, real-time pH monitoring. The positively charged rhodamine selectively targets mitochondria via electrostatic interactions with their negatively charged membranes. Both probes exhibit high sensitivity across a broad pH range, and probe **A** was employed to visualize transient pH shifts within mitochondria. Additionally, probe $\mathbf{AH}^+$ possesses the additional attribute of monitoring

viscosity at low pHs. By overcoming the limitations of conventional pH probes, probes **A** and potentially **B** provide robust tools for investigating mitochondrial function, viscosity, and stress responses in living cells. This work demonstrates their potential for advancing our understanding of oxidative stress, hypoxia, mitophagy, and related pathological processes, offering valuable insights into cellular health and disease.

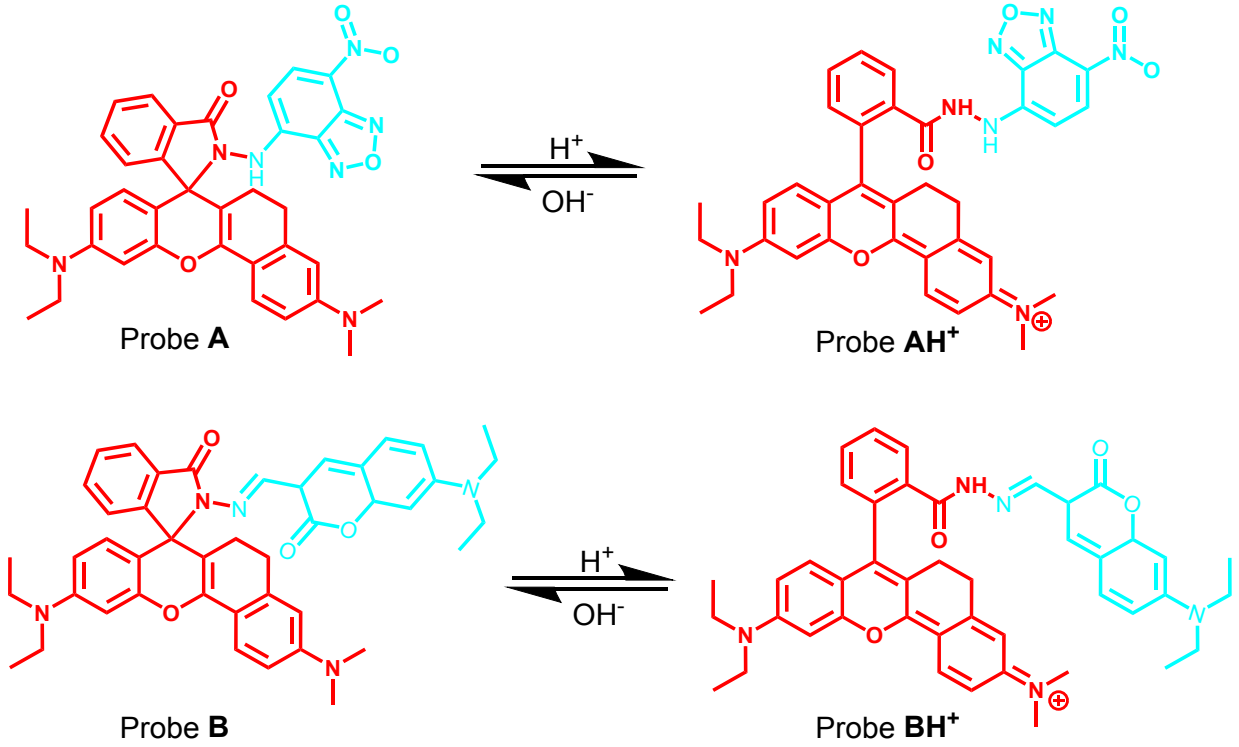

Scheme 1. Structures of probes **A**, **AH**$^+$, **B**, and **BH**$^+$ illustrating pH-dependent equilibria.

Experimental Section

Details of all reagents, instrumentation, solution preparations, and the synthesis procedure are provided in the Supporting Information (SI).

Optical Study

A stock solution (1.5 mM) of each probe was prepared in 3.0 mL of DMSO for optical measurements. For each measurement, 20 µL of the stock solution was diluted in 900 µL of DMSO, with the pH adjusted using either citrate–phosphate buffers (0.1 M) or carbonate–bicarbonate (0.2 M) buffer solutions at various pH levels (2100 µL). All optical measurements were performed in 1 cm path-length quartz cuvettes across a pH range of 2.60 to 9.07. The UV-visible spectrum of each pH-adjusted solution was recorded, and the wavelength closest to maximum absorption was used for excitation during fluorescence measurements.

Cellular fluorescence imaging

Complete growth media was prepared using Dulbecco's Modified Eagle's Medium (DMEM) with a glucose concentration of 1 g/L, fetal bovine serum (FBS), penicillin, and streptomycin in a 5:1:1 ratio. HeLa cells were cultured in this growth media under a 5% CO_2 and 95% air atmosphere at 37°C in cell culture dishes. Before cellular imaging, cells were seeded in

confocal dishes with the growth media for 24 hours and then incubated with 10 μM of probe **A** for 30 minutes. Cells were washed three times with the growth media.

To monitor intracellular pH at various levels, cells stained with probe **A** were further incubated for 10 minutes at 37°C in different pH buffers containing 10 μM nigericin, which equilibrates the intracellular pH with buffer pH. The color scale presented in Figs. 4–7 and 9 serves as an approximate pH reference, qualitatively aligned with the pH values indicated on the left side of Fig. 4. This scale is generated automatically by the ImageJ software during the computation of "Ratiometric Image" columns, which display pseudocolored representations of the ratio between red (Channel II) and green (Channel I) fluorescence intensities. The images are first split into their respective channels, and the red channel is divided by the green. To enhance visual contrast, the FIRE-Look-Up Table or FIRE-LUT is applied, enabling subtle intensity differences that might otherwise be imperceptible in grayscale to be readily distinguished.

In this color mapping, FIRE-LUT assigns colors to pixel values based on a gradient: lower values correspond to cooler tones (e.g., black), while higher values map to warmer tones (e.g., yellow). This visualization approach highlights the pH sensitivity of probe **A**, as reflected by the variations in pseudocolor intensity across different conditions. The resulting pseudocolor images can be interpreted semi-quantitatively by referencing the corresponding color bar, allowing for approximate estimation of local pH values. For instance, the bright yellow regions observed at pH 3.3 in Fig. 4 suggest a highly acidic environment. However, at this pH, the ratiometric image suffers from reduced intensity due to the scarcity of signal in Channel I, leading to division by zero in some regions—manifested in the software as "NaN" (Not a Number) values.

Oxidative stress on intercellular pH fluctuation was investigated by chemical treatments with redox-active chemicals. Cells incubated with the probe were further treated with hydrogen peroxide (H_2O_2, 100 μM), carbonyl cyanide 4-(trifluoromethoxy) phenylhydrazone (FCCP, 10 μM), and N-acetylcysteine (NAC, 1 mM) for 30 mins in pH 7.4 DMEM.

Cells stained with probe **A** were washed and the starvation test was performed in a serum-free medium at various time intervals (0, 45, 75, 120, and 150 mins.).

A chemical hypoxia test was conducted by incubating cells with varying concentrations of $CoCl_2$ (0, 50, 100, and 150 μM) before probe addition. After incubation, confocal dishes were washed three times with complete growth media, followed by the addition of 10 μM of the probe and a 30-minute incubation. The dishes were then washed again three times with complete growth media, and 1 mL of growth media was added before imaging. Results from different $CoCl_2$ concentrations are compared with images from control cells not treated with $CoCl_2$. Ratiometric fluorescence imaging was captured between 425-525 nm (green channel) with excitation at 405 nm, and between 600-700 nm (red channel) with excitation at 559 nm.

For the colocalization study, probe **A** and IR780 were added to the cultured cells in confocal dishes and incubated for 30 mins. After washing three times with complete growth media, fluorescence images were captured immediately. The fluorescence of IR780 is collected at 700–800 nm with excitation at 635 nm (Alexa Fluor 635).

The nystatin tests, Fig. 11, consisted of incubating HeLa cells with 10 μM of probe **A** in a standard culture medium for 30 mins. The cells were washed three times with standard culture medium and incubated with nystatin (0, 10, 20, and 30 μM), 500 μL standard culture medium, and 500 μL of pH buffer (pH = 3.8) for 10 mins. The green channel (Channel I) was employed to

detect visible fluorescence from probe **A** in the emission range of 425–525 nm, while the red channel (Channel II) was used to capture near-infrared fluorescence between 600–675 nm.

In Fig. 12, the intensity measured at pH 3.8 for the control used identical parameters to those for the standard pH determinations, specifically HV (Alexa Fluor 405 = 517 V, Alexa Fluor 568=420 V), Gain (Alexa Fluor 405 = 3x, Alexa Fluor 568=3x), Offset (Alexa Fluor 405 = 99 %, Alexa Fluor 568=9 %), and laser (Alexa Fluor 405 = 54 %, Alexa Fluor 568=40 %). DIC60 condense, LSM mirror, and PLAPON n60x O objective lens on the Olympus FluoView FV1000 Confocal Microscope.

Fruit fly studies

Wingless *D. Melanogaster* flies from a commercial source were utilized for this study. 250 to 500 adult flies were placed into a container with agar plates at the bottom; the agar plates were coated with a Baker's yeast paste and were supplemented with Baker's yeast, sucrose, and malt powder. The flies were left in this container for 24 to 48 hours until eggs were laid, and larvae hatched. The larvae were gathered by flooding the agar plate with PBS buffer and rubbing the plate with a swab to release the larvae from the plate. The larvae solution was then serially diluted to remove particulate and other contaminants from the solution. The larvae were then collected from under a microscope using a pin when they were in the instars 1 or 2 stage of development. 125 to 150 larvae were collected and were placed into a well plate. The larvae were divided between 5 wells, each containing 350 μL of buffer solutions with increasing pH levels. The larvae were allowed to incubate in the pure buffer solution for 1 hour. Then, 50 μL of a 10 μM solution of probe **A** was added to each plate. The larvae were allowed to further incubate for 4 hours. The larvae were then removed from each well, placed onto a glass slide, and washed twice with distilled water. A cover slip was then applied for fluorescence imaging using 405 and 559 nm excitation.

Theoretical Calculations

Optimization and frequency calculations for probe **A** were performed at the APFD/6-311+G(d) level[37] using the Gaussian 16 suite[38] of programs. No imaginary frequencies are observed. The first ten excited states are evaluated through TD-DFT[39] optimizations within a Polarizable Continuum Model[40] (PCM) of water. The results are analyzed using GausView[41] for all additional data but figures were generated using Mercury.[42] XYZ coordinates and specific conditions for the pKa calculations are provided in the SI.

Results

Design and Synthesis of probes A and B

A rhodamine acceptor connected with two different donors was designed and synthesized for pH detection yielding probes **A** and **B**. The synthetic routes are presented in Scheme 2 and the syntheses of compounds **1** and **2** are described in Supporting Information. Compound **3**, a

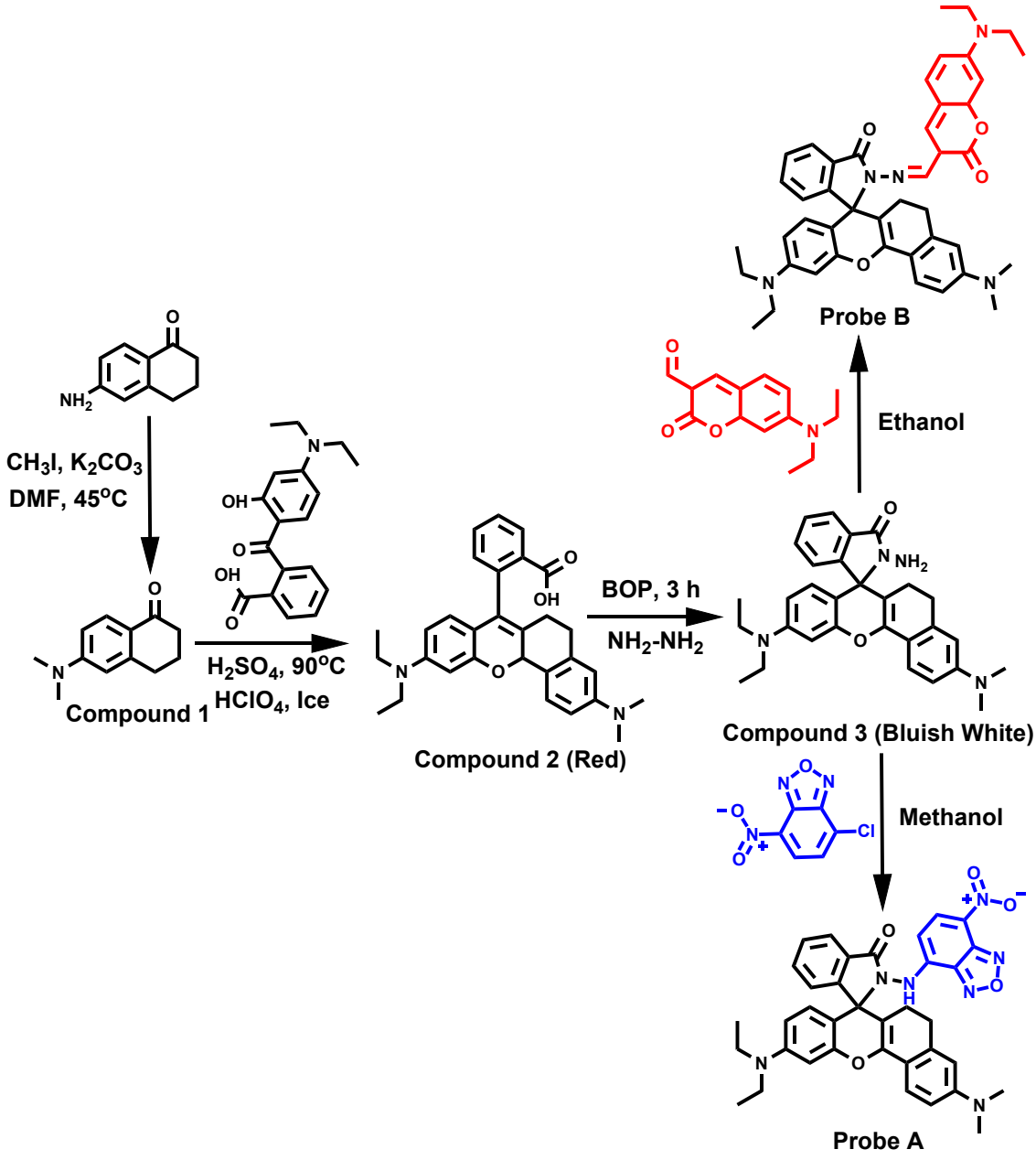

Scheme 2. Synthetic route to probes **A** and **B.**

rhodamine dye containing an amine residue was synthesized through a two-step process. Initially, a condensation reaction was carried out between 2-(4-(diethylamino)-2-hydroxybenzoyl)benzoic

acid and 6-amino-3,4-dihydro-1(2H)-naphthalenone in concentrated sulfuric acid. This was followed by cyclic amide formation with hydrazine, facilitated by the coupling reagent benzotriazol-1-yl-oxy-tris-(dimethylamino)-phosphonium hexafluorophosphate (BOP). The rhodamine-bearing amine, receptor **3**, is then connected to 7-nitrobenzofurazan, and 7-(diethylamino)-2-oxo-3,8a-dihydro-2H-chromene-3-carbaldehyde donor to prepare probes **A** and **B**, respectively. The structures of the synthesized probes in the closed spirolactam state are confirmed by ^{1}H and ^{13}C NMR, ESI-LCMS, MALDI, and FTIR spectra which are detailed as Supporting Information. Evidence of the open state is in the [1] in the presence of 1 and 2 equivalents of trifluoracetic acid where two NH signals (closed, **A**, δ 10.96 and open, **AH**$^{+}$, δ 11.04 and 11.45) are observed, Figs. S5a-S5c. We anticipated that the extended π-conjugation system within the rhodamine core, coupled with distinctly visible fluorophores as donor groups, would exhibit ratiometric fluorescence emission via a Förster Resonance Energy Transfer (FRET) mechanism, Scheme 3.

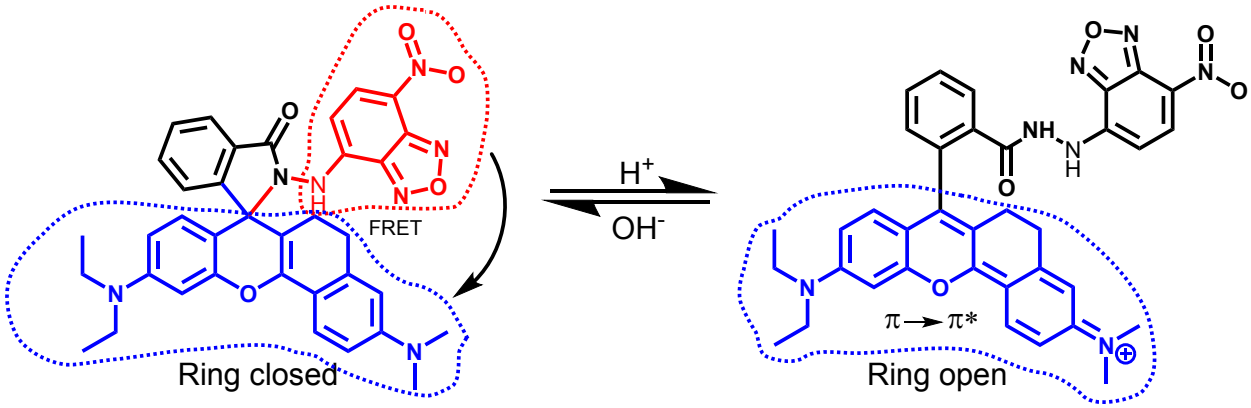

Scheme 3. FRET and π → π* absorption mechanisms within probes **A** and **AH**$^{+}$.

UV-Vis and Fluorescence spectra characteristics

The absorption and emission spectra of both probes were recorded in buffered solutions containing 30% DMSO as co-solvent. Under acidic conditions, the absorption peaks of probe **AH**$^{+}$ at about 621 nm and 445 nm gradually decrease in intensity as the pH increases, Fig. 1 (a). Upon reaching a pH of 6.29, a new absorption peak emerged at 482 nm due to the formation of probe **A**, which progressively increased in intensity with further increases in pH. A broad peak is observed at 320 nm, which gradually increases in intensity and sharpens into a narrower band as the pH increases. Upon excitation at 370 nm, an emission peak at 660 nm is observed for probe **AH**$^{+}$ at pH 3.50 (Fig. 1b). This emission is attributed to the acid-activated open form of the spirolactam, which generates a conjugated π-system. As the pH increases, the intensity of the emission peak at 660 nm steadily decreases and undergoes a blue shift to 645 nm, indicating the transition to the ring-closed form of the spirolactam. At a high pH of 9.10, an emission band appears at 465 nm, attributed to the presence of nitrobenzofurazan moieties. The intensity of the 465 nm peak steadily decreases with a reduction in pH, due to energy transfer from the nitrobenzofurazan moieties to the spirolactam via a Förster Resonance Energy Transfer (FRET) mechanism.

The absorption spectrum of probe **B,** containing the 7-(diethylamino)-2-oxo-3,8a-dihydro-2H-chromene-3-carbaldehyde donor group, is also pH dependent and, under acidic conditions at pH 2.60, a large absorption indicative of probe $\mathbf{BH^+}$ at 440 nm with a shoulder at 376 nm is observed, Fig. S15. This transforms into two large absorptions at 454 and 329 nm under basic conditions. Under basic conditions, probe **B** displays a broad fluorescence band at 570 nm under excitation at 325 nm, Fig S15. Decreases in pH result in increases in the intensity of the coumarin emission signal at 510 nm, while the orange-colored broad emission at 570 nm decreases completely. This is caused by ring opening of the spirolactam bond upon protonation resulting in extended conjugation within the coumarin moiety. The pKa values for probes **A** and **B** are determined to be 4.43, and 4.14 respectively, Fig. S16. While both probes exhibit ratiometric fluorescence responses to pH changes, those for probe **A** are more pronounced than those for probe **B** judging from their emission spectra, Figs. 1(b) and S15.

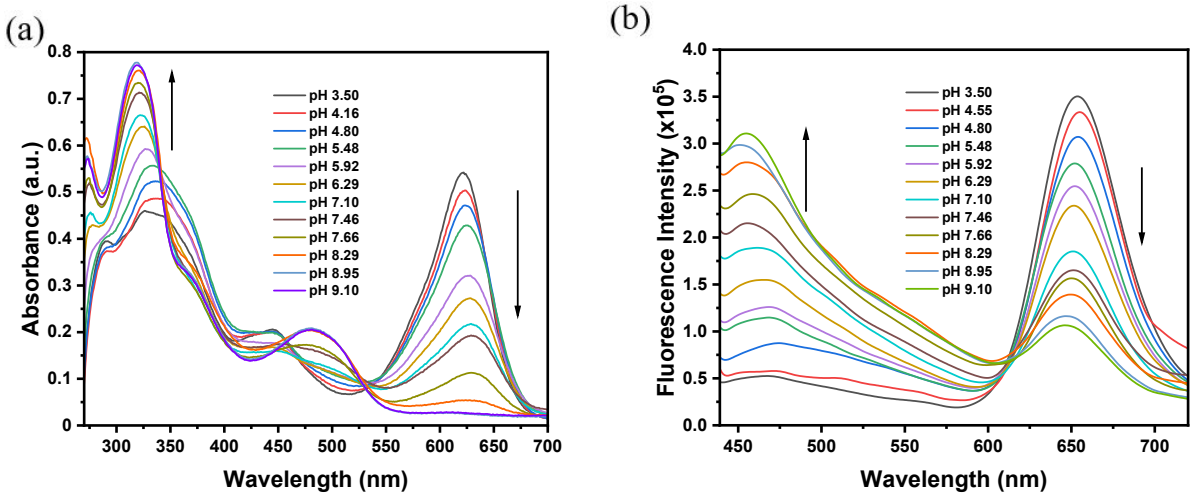

Figure 1. (a) Absorption and (b) fluorescence spectra with excitation at 370 nm of probe **A** (10 μM) recorded in various pH buffer solutions containing 30% DMSO.

Theoretical Calculations:

Theoretical calculations (full details in SI) were conducted to assess both the changes in geometry that result from the protonation of probes and the nature of the electronic transitions. In probe **A**, Fig. S20, the two benzene rings attached to the central pyran moiety of the rhodamine are twisted by 19.2°, whereas in probe **B**, Fig S29, this interplanar angle is smaller at 13.6°. The dialkylaminorhodamine section is joined via an almost perpendicularly arranged aminoisoindolin-1-one group in probe **A** (89°) to the planar 7-nitrobenzofurazan moiety and to a diethylaminochromene group which is oriented away from the dimethylamino section of the rhodamine in probe **B** (86.8°). The arrangement enforces approximate co-planarity between the rhodamine and the 7-nitrobenzofurazan moieties separated by a distance of 3.167 Å in probe **A**, Fig S20. Protonation of the N atom in the pyrrolidin-2-one ring in **A** to produce $\mathbf{AH^+}$ results in a reduction of the twist between the two benzene rings in the rhodamine section to 14.9° which is caused by increased π-conjugation and planarity in the central pyran. In probe $\mathbf{AH^+}$, the C-C atom linkage between the aminoisoindolin-1-one group and the pyran section of the rhodamine is rotated ~180° compared to probe **A**, resulting in interplanar angles between these planes of 77.8° and those

between the rhodamine and the nitrobenzofurazan is at 57.8°. This shows that protonation of probe **A** resulted in probe **AH**$^+$ adopting a more conjugated planar rhodamine moiety producing the shift in the absorbance to longer wavelengths, Fig. 1. This conformational difference is shown in an overlay diagram of one of the benzene rings in the rhodamine section for the two probes, Fig. S21, which depicts a similar rhodamine section and the dramatic difference in the position of the nitrobenzofurazan moieties. The difference in conformation between probes **B** and **BH**$^+$ is depicted in an overlay diagram, Fig, S30. Protonation of probe **B** results in dramatic changes in the geometry as the chromene moiety is arranged stacked over the dimethylamino-rhodamine section, perhaps indicative of π–π interactions, Fig. S34. The interplanar angles of the outer benzene rings in the rhodamine moiety have increased from 13.6° in **B** to 18.0° in **BH**$^+$, Fig. S34, and the aminoisoindolin-1-one group is now at 74.5° with respect to the central pyran to accommodate this π–π interaction.

Selected calculated bond distances are tabulated in Table 1. The shorter C_1-N_2 and N_2-N_3 distances between the probes' series are due to the C_1-N_2 double bond in probe **B** which may perhaps indicate increased conjugation to the chromene moiety. The C_4-C_5 and C_5-C_6 distances show slight increases upon protonation with C_6-C_7 and C_7-C_8 decreasing due to increases in bonding and conjugation. This suggests that changes in the rhodamine conformers of the probes are responsible for the change in the emission wavelength observed experimentally upon protonation.

Table 1. Comparison of selected bond distances between probes **A**, **AH**$^+$, **B**, and **BH**$^+$.

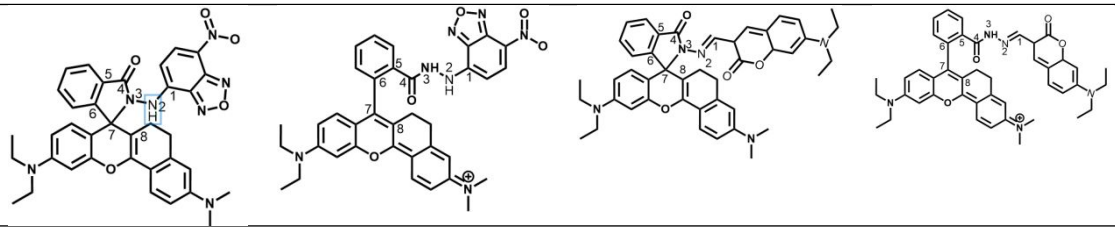

Probe	A	AH$^+$	B	BH$^+$
C_1-N_2	1.368	1.360	1.277	1.272
N_2-N_3	1.383	1.370	1.350	1.358
N_3-C_4	1.374	1.372	1.375	1.366
C_4-C_5	1.480	1.492	1.474	1.502
C_5-C_6	1.390	1.405	1.386	1.406
C_6-C_7	1.507	1.482	1.508	1.487
C_7-C_8	1.497	1.407	1.496	1.390

There were slight differences (within the allowed ranges[43]) in the calculated absorption conducted at the APFD/6-311+G(d) level with probe **A** containing major absorptions at 478 and 397 nm (expt. 482 and 320 nm), probe **AH**$^+$ at 528, and 392 nm (expt. 621 and 445 nm), probe **B** 416 and 324 nm (expt. 520 and 370 nm), and probe **BH**$^+$ at 528 nm (expt. 621 and 438 nm). The Tauc plot[44] contained values for the bandgap for probes **A** and **AH**$^+$ at 2.29 and 1.88 eV, Fig. S14,

and these differed from the calculated values obtained for the HOMO to LUMO transitions at 2.08 and 2.39 eV respectively. Inspection of the current density diagram for transition ES 2 (478 nm) for probe **A**, Fig. 2, indicates that the electronic transition originates from the rhodamine region ending up on the nitrobenzofurazan moiety. Orbitals on the bridging aminoisoindolin-1-one moiety are not involved with this transition which would suggest a FRET mechanism is operative. The lower wavelength transition on probe **A** (397 nm) also involves similar transfer to that in ES 2 except that π–π* transfer on the nitrobenzofurazan moiety contributes, Fig. S24. Protonation of the distal N atom in the bridging aminoisoindolin-1-one group in probe **A** results in an increased separation of the rhodamine and the nitrobenzofurazan groups reducing the possibility of FRET transfer. Indeed, a main transition, ES 2, (528 nm), is a π–π* transfer localized on the rhodamine orbitals with some involvement of orbitals on the aminoisoindolin-1-one group. A second transition, ES 6, (362 nm) is mostly (84%, Fig. 2) a π-π* transfer localized on the nitrobenzofurazan moiety, Fig. 2, with a much smaller contribution (10%) restricted to π-π* transfer localized on the rhodamine group. For probe **B**, a weak transition (416 nm) based on movement of electron density from the diethyl group on the chromene towards the bridging group is calculated, Fig. 2. The main transition at 324 nm originated from the dimethyl group attached to rhodamine moiety towards the center part of the rhodamine and also involving lobes on the bridging aminoisoindolin-1-one group, Fig. 2 and S33. Interestingly, a large transition for probe $\mathbf{BH}^+$ at 528 nm was based on movement from the diethyl section on the rhodamine towards the center and almost completely localized on this group.

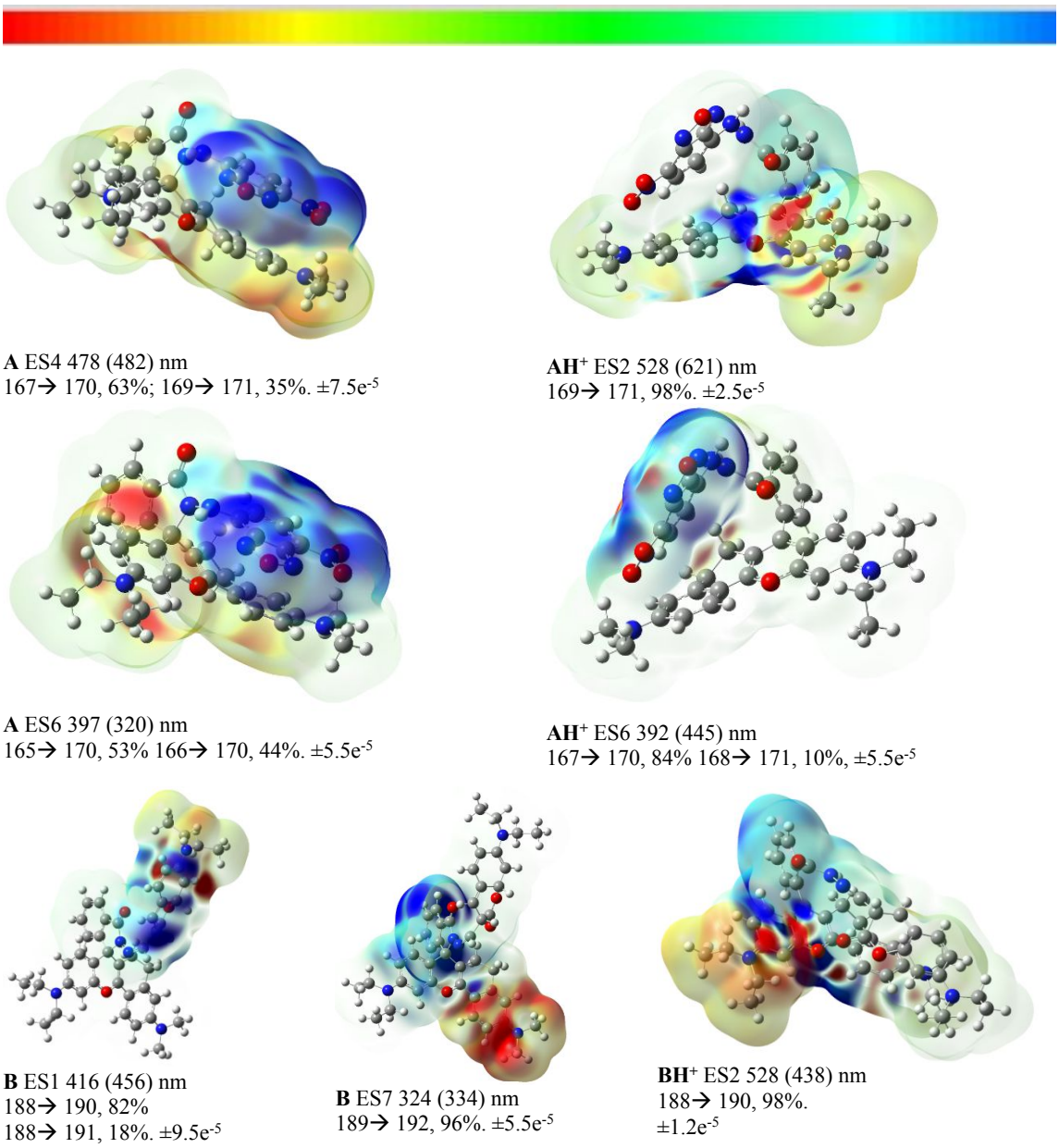

Figure 2. Current density difference drawings as isosurfaces for probes **A**, **AH**$^+$, **B**, and **BH**$^+$. The number of excited states (ES), the calculated (and experimental) wavelengths, and the transitions together with percentage contributions are listed. The range values for the color scale illustrated at the top of the figure are also listed. Drawings of the numbered LCAOs are available in the Supporting Information.

Fluorescence Imaging in HeLa Cells

Probe **A**, Fig. 1, exhibited more clearly defined ratiometric emissions compared to probe **B**, Fig. S15, which led to the selection of probe **A** for fluorescence imaging in live cell assays. The probes enter the cells through either endocytosis or passive diffusion; however, the exact mechanism of uptake has not been conclusively determined.[45] The subcellular distribution was examined by staining HeLa cells with probe **A** and a commercially available mitochondria-specific

dye (IR-780)®. The intracellular fluorescence of the probe shows that the probe predominantly localizes in the mitochondria, as demonstrated by the strong co-localization of probe **A** red emission with IR-780's magenta emission (Pearson correlation coefficient (PCC) = 0.931, Fig. 3). A similar measurement using lysosome tracker (probe **5**)[46] resulted in a PCC of 0.59, Fig. S39. Therefore, the probe effectively and selectively stains mitochondria with high correlation but does have a low to moderate correlation with lysosomes in living cells. Notably, probe **A** can be employed to monitor mitophagy, as demonstrated by its response to rapamycin treatment in HeLa cells.[47] Upon rapamycin incubation, a marked increase in the PCC between probe **A** and lysotracker **5**[46] was observed, rising from an initial value of 0.64 to 0.92 after 120 minutes (Fig. S40). This increase is attributed to rapamycin-induced mitophagy, during which mitochondria are engulfed by lysosomes, leading to the co-localization and subsequent encapsulation of probe **A** within the autolysosomal structures.

The positively charged ring-open forms of probes **A** and **B** remain in equilibrium with their closed-ring counterparts even at pH values exceeding 8.5, as shown in Figs. 1(b) and S15(b), respectively. The open cationic species becomes electrostatically sequestered by the negative mitochondrial membrane potential and is unable to diffuse out. This drives the equilibrium toward regeneration of the open form, thereby promoting selective accumulation of the probe within mitochondria. Notably, probe **A** exhibits a slightly positive zeta potential[48] of 0.466 mV, indicating a net surface charge, Fig. S41.

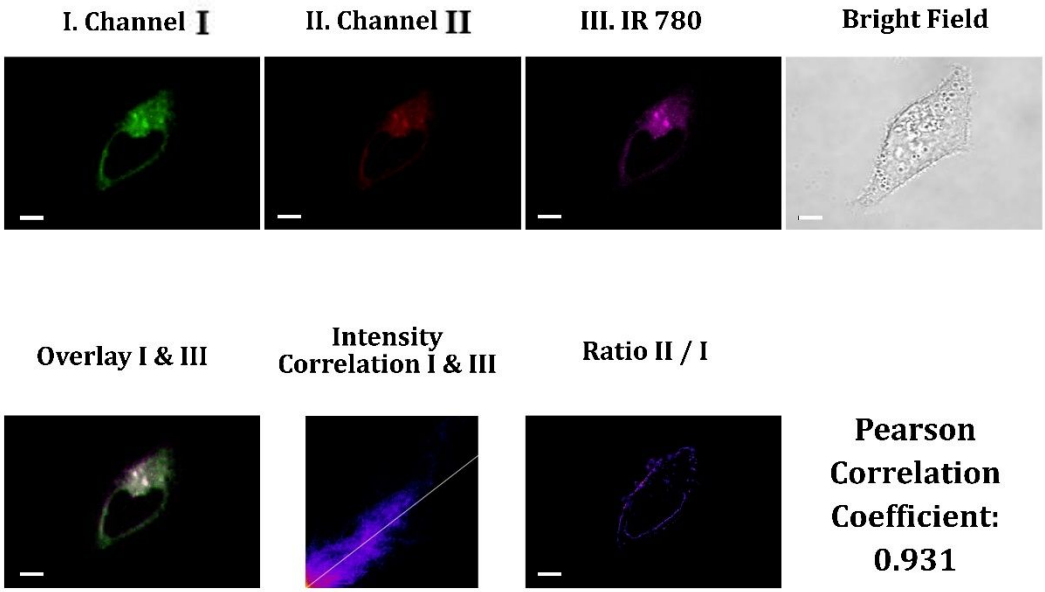

Figure 3. Fluorescence images of HeLa cells were captured after a 30 min incubation with 10 μM probe **A** and 10 μM of IR-780 dye. The green channel (I) was used to observe the visible fluorescence of probe **A** in the 425-525 nm range, while the red channel (II) captured near-infrared fluorescence from probe **A** (600-700 nm). The green channel employed Alexa Fluor 405 (excitation at 405 nm), and the red channel utilized

Alexa Fluor 568 (excitation at 559 nm). The magenta channel (III) was used to detect near-infrared fluorescence from the mitochondria-specific dye (IR-780) in the 700-800 nm range, with Alexa Fluor 635 (excitation at 633 nm). Scale bars represent 20 μm. A PCC value of 0.929 was obtained for the channel II / IR 780 overlay.

The effect of pH on living cells in the presence of probe **A** was investigated by capturing fluorescence images of HeLa cells incubated with five different pH buffers. The intracellular fluorescence of probe **A** was subsequently analyzed. As shown in the laser confocal microscopy images, Fig. 4a, strong red fluorescence (Channel II, 600-700 nm) was observed when cells were treated with a pH 3.3 buffer, with minimal green fluorescence (Channel I, 425-525 nm) detected. As the intracellular pH increased (5.6, 6.9, 8.0, and 9.0), green fluorescence intensified while red fluorescence diminished. An incremental change in the intensities of green and red fluorescence, observed in opposite directions, indicates the pH-dependent response of the probe within living cells. This behavior is consistent with the proportional fluorescence responses of the probe in various pH buffer solutions. The merged images of cells containing the probe exhibit a distinct color transition from red to green as the intracellular pH increases from 3.3 to 9.0. The ratiometric images, obtained using the ImageJ image calculator with pseudo-coloring, show a color shift from yellowish-purple to bluish-purple corresponding to changes in intracellular pH from 3.3 to 9.0. Additionally, the histogram, Fig. 4b provides quantitative data demonstrating a regular increase in green channel intensity and a decrease in red channel intensity as the pH value rises. The ratio of red to green fluorescence (I_2/I_1) decreases as the pH increases from 3.3 to 9.0. These results confirm that probe **A** is cell membrane-permeable and responsive to pH changes, effectively monitoring fluctuations in intracellular pH levels in live cells. The probe's sensitivity to pH variations enables it to provide real-time insights into the cellular environment. The probe exhibits a ratiometric on–off fluorescence response upon mitochondrial acidification, enabling accurate pH measurement within living cells. In contrast to other mitochondria-targeted probes with single-wavelength emission profiles reported in the literature, Table S9, our rhodamine-based probe features a low pK_a and ratiometric emission behavior. These attributes enhance its sensitivity and suitability for monitoring dysfunctional mitochondria undergoing mitophagy.

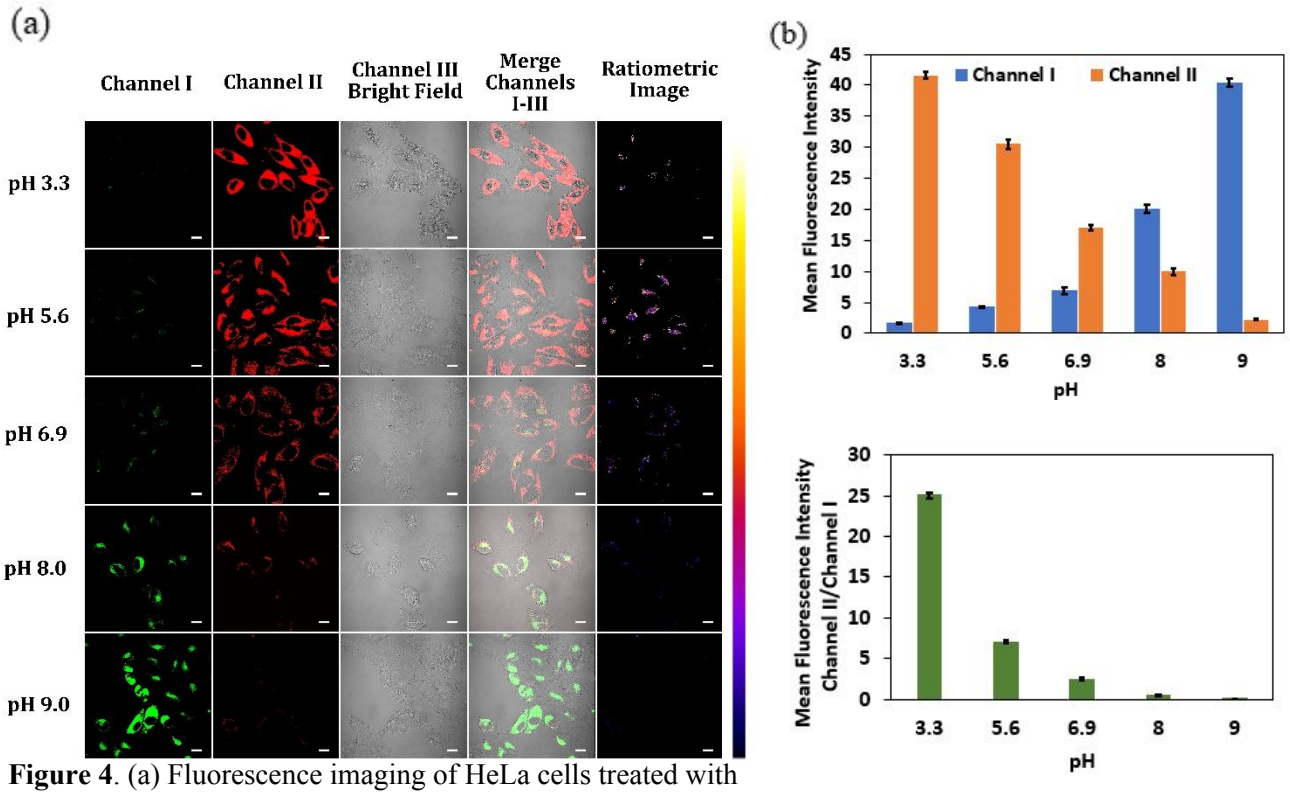

Figure 4. (a) Fluorescence imaging of HeLa cells treated with 10 μM of probe **A** in a series of pH-adjusted buffers, each supplemented with 10 μM nigericin. The green fluorescence channel (I) captures the emission of probe **A** within the range of 425–525 nm, while the red fluorescence channel (II) detects near-infrared emission spanning 600–700 nm. Green fluorescence was visualized using Alexa Fluor 405 (excitation at 405 nm), and red fluorescence was monitored using Alexa Fluor 568 (excitation at 559 nm). Scale bars in all images represent 50 μm. (b) Histograms illustrating the emission intensities from channel I (green) and channel II (red) (top), and the fluorescence intensity ratio of channel II to channel I for probe **A** in HeLa cells (bottom) under varying pH conditions, as quantified from the fluorescence images with SD bars based on n=3.

Mitophagy, a specialized form of autophagy, plays a critical role in maintaining cellular homeostasis and metabolic efficiency by selectively removing damaged mitochondria and recycling their components through a lysosome-dependent pathway.[49] During this process, mitophagosomes fuse with nearby lysosomes to form autolysosomes, where mitochondrial constituents are degraded, resulting in a reduction of pH within the mitochondria. Here, we utilized probe **A** to monitor mitophagy by assessing pH changes within mitochondria. For starvation-induced stimulation, HeLa cells were incubated with 10 μM of probe **A** in serum-free DMEM for varying durations, ranging from 0 to 150 minutes.

Fluorescence imaging revealed a progressive increase in red-channel fluorescence intensity (channel II) and a corresponding decrease in green-channel fluorescence intensity (channel I) over the 150-minute starvation period, as shown in Fig. 5(a). A noticeable color shift from reddish-green to yellowish-red was observed in the merged images of channels I and II. The ratio images of channel II to channel I displayed a transition from bluish-purple to yellowish-purple after 150

minutes of nutrient deprivation. The histogram in Fig. 5(b) quantitatively illustrates the fluorescence intensity changes in Channel I, Channel II, and the ratio of Channel II to Channel I, based on the acquired fluorescence images. The increasing ratio of channel II to channel I reflects a decrease in pH within the autolysosomes over time. This pH reduction, induced by mitophagy triggered under nutrient deprivation, caused protonation and subsequent ring opening of probe **A**, thereby enhancing the fluorescence intensity in the red channel over time.

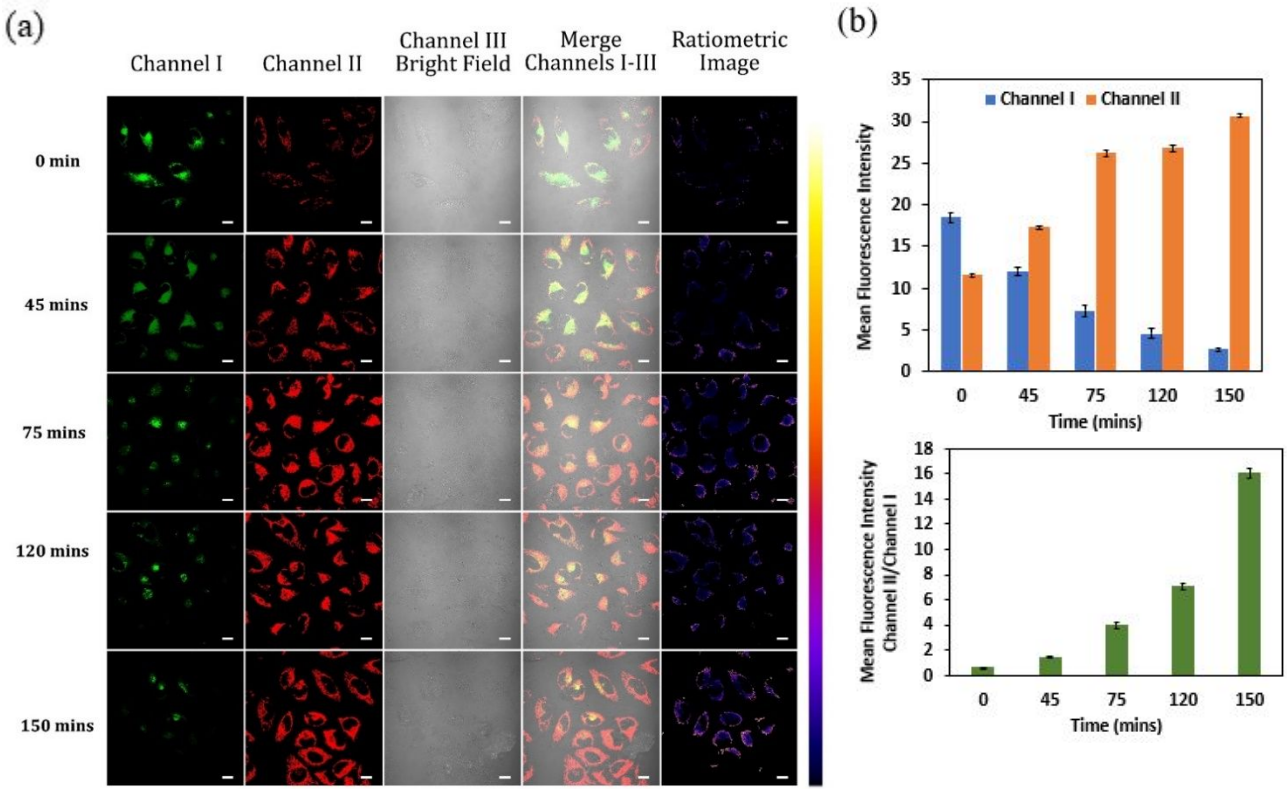

Figure 5. (a) Fluorescence imaging of HeLa cells was performed using 10 μM of probe **A** incubated in a serum-free medium for varying time intervals. The green channel (Channel I) was employed to detect the visible fluorescence of probe **A** in the range of 425–525 nm, while the red channel (Channel II) captured near-infrared fluorescence between 600–675 nm. Green fluorescence was visualized using Alexa Fluor 405 (excitation at 405 nm), and red fluorescence was monitored using Alexa Fluor 568 (excitation at 559 nm). All fluorescence images are presented with a scale bar of 50 μm. (b) Histograms depicting the emission intensities of Channel I (green) and Channel II (red) (top), and the fluorescence intensity ratio of Channel II to Channel I for probe **A** in HeLa cells (bottom) over different time intervals, as quantified from the fluorescence images with SD bars based on n=3.

Oxygen is essential for most living organisms, functioning as a scavenger to remove harmful electrons and hydrogen ions generated during mitochondrial oxidative phosphorylation.[50] A condition of low oxygen levels (typically below 2%), known as hypoxia, can occur in specific organs, tissues, or cell types. Hypoxia is implicated in the pathology of numerous major diseases, including cancer, cardiovascular diseases, chronic kidney disease, metabolic disorders, preeclampsia, and endometriosis.[51] In particular, hypoxia in cancer cells plays a critical role in tumor progression, angiogenesis, metastasis, and drug resistance.[52]

Probe **A** was employed to monitor hypoxic conditions within HeLa cells. A hypoxic environment inside the cells was simulated using cobalt chloride ($CoCl_2$),[53] which stabilizes hypoxia-inducible factors (HIFs). As the concentration of $CoCl_2$ increased from 0 to 150 μM, a corresponding increase in red-channel fluorescence intensity and a decrease in green-channel fluorescence intensity were observed, as shown in Fig. 6(a). The merged images of Channels I and II revealed a shift in color from yellowish-green to yellowish-red. Ratiometric images demonstrated an increase in yellowish-purple intensity with rising $CoCl_2$ concentrations.

The histogram in Fig. 6(b) illustrates the mean fluorescence intensities of Channel I (green), Channel II (red), and the ratio of Channel II to Channel I. The ratio of Channel II to Channel I increased with higher $CoCl_2$ concentrations, indicating intracellular acidification and rhodamine ring opening of probe **A** under hypoxic conditions. These findings confirm that low oxygen levels lead to increased H^+ concentrations and reduced pH, which can be effectively monitored using probe **A** in live cells.

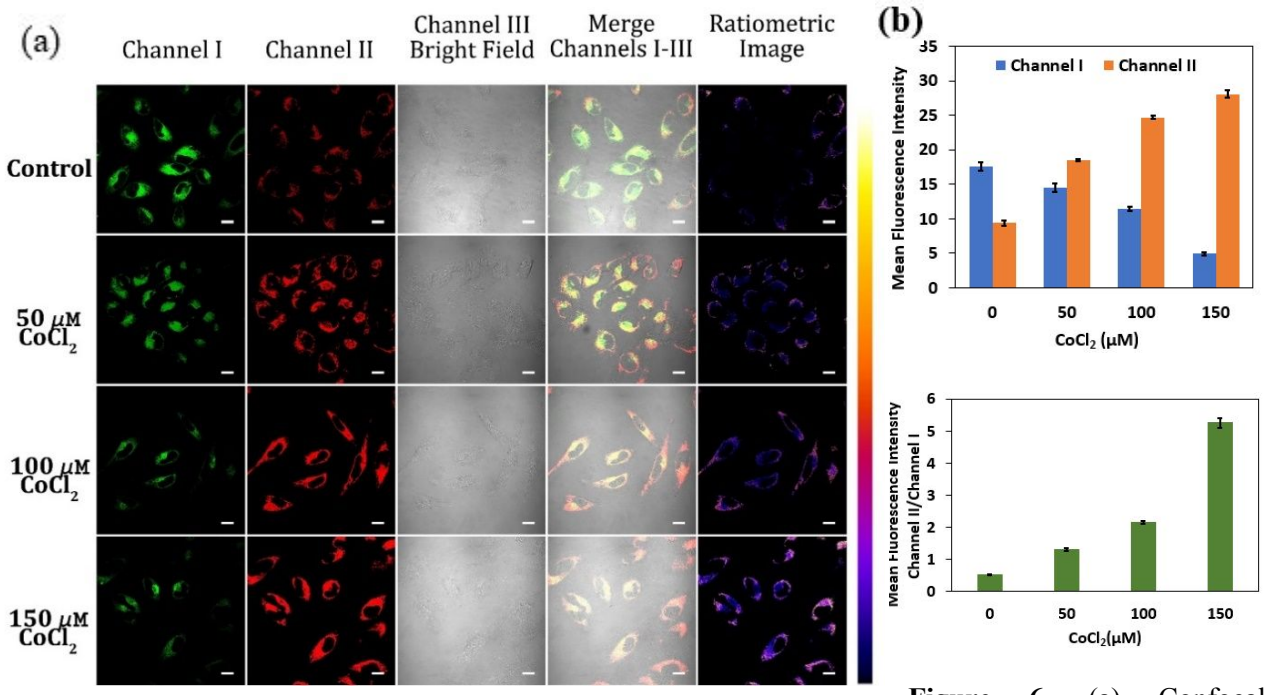

Figure 6. (a) Confocal fluorescence microscopy images of HeLa cells incubated with 10 μM of probe **A** under varying hypoxic conditions induced by $CoCl_2$ at concentrations of 0, 50, 100, and 150 μM. The green channel (Channel I) was used to detect the visible fluorescence of probe **A** in the emission range of 425–525 nm, while the red channel (Channel II) captured near-infrared fluorescence in the range of 600–675 nm. Green fluorescence was visualized using Alexa Fluor 405 (excitation at 405 nm), and red fluorescence was detected using Alexa Fluor 568 (excitation at 559 nm). All images are presented with a scale bar of 50 μm. (b) Histograms depicting the emission intensities of Channel I (green) and Channel II (red) (top), and the fluorescence intensity ratio of Channel II to Channel I for probe A in HeLa cells (bottom) under different $CoCl_2$ concentrations, as quantified from the fluorescence images with SD bars based on n=3.

The mitochondrial pH in living cells can be significantly altered by specific chemical stimuli. To assess the performance of probe **A** in monitoring mitochondrial pH changes, HeLa cells stained with probe **A** were treated with carbonyl cyanide 4-(trifluoromethoxy)phenylhydrazone (FCCP), N-acetyl-L-cysteine (NAC), and hydrogen peroxide (H_2O_2). FCCP is a protonophore that stimulates respiration, increases oxygen consumption, and disrupts the proton gradient across the inner mitochondrial membrane, thereby uncoupling mitochondrial oxidative phosphorylation.[54] Fluorescence microscopy images of probe **A**-stained HeLa cells following FCCP treatment were collected and are presented in Fig. 7(a). After 20 minutes of treatment with 10 μM FCCP in DMEM at pH 7.4, a marked increase in fluorescence intensity in the red channel (Channel II) and a corresponding decrease in the green channel (Channel I) was observed compared to the untreated control. This indicates that the mitochondrial membrane potential was disrupted, resulting in a slight decrease in pH due to mitochondrial acidification. The ratio of Channel II to Channel I increased significantly, from 0.55 in the control to approximately 3.38 after FCCP treatment, as shown in Fig. 7(b).

NAC, a precursor to glutathione (GSH), reduces oxidative stress and mitigates mitochondrial dysfunction.[55] Fluorescence imaging of probe **A**-stained HeLa cells treated with NAC also demonstrated mitochondrial acidification, characterized by decreased fluorescence in the green channel and increased fluorescence in the red channel, as shown in Fig. 7(a). NAC, acting as a proton donor, increased the ratio of Channel II to Channel I from 0.55 in the control to approximately 1.87, as illustrated in Fig. 7(b).

Furthermore, probe **A**-stained HeLa cells were treated with hydrogen peroxide (H_2O_2). H_2O_2 is known to disrupt H^+ ion distribution by impairing the vacuolar proton pump (V-ATPase), which can lead to mitochondrial acidification through ATP hydrolysis.[56] Furthermore, the oxidation of H_2O_2 generates intracellular hydroxyl free radicals, contributing to intracellular acidosis.[57] These hydroxyl radicals also inhibit glycolysis, promoting ATP hydrolysis and further reducing intracellular pH.[58] Following H_2O_2 treatment, fluorescence imaging of probe **A**-stained HeLa cells revealed a substantial increase in red-channel fluorescence intensity (Channel II) and a corresponding decrease in green-channel fluorescence intensity (Channel I), as shown in Fig. 7(a). This indicates significant intracellular acidification due to H_2O_2 exposure. The merged images of Channels I and II demonstrate a shift in color from green to yellowish-red after H_2O_2 treatment. The histogram in Fig. 7(b) shows that the ratio of Channel II to Channel I increased markedly from 0.55 in the control to approximately 2.67 after H_2O_2 treatment, further confirming the acidification of the intracellular environment induced by H_2O_2.

Finally, the emission intensities of probes **A** and **B** remained unaffected in the presence of 100 μM peroxynitrite, hydrogen peroxide (H_2O_2), and 100 μL of hydrogen sulfide (H_2S) gas in PBS solution, as shown in Fig. S42. These experiments were conducted to evaluate the probes' stability in the presence of reactive nitrogen species (RNS), reactive oxygen species (ROS), and reactive sulfur species (RSS). Based on these results, we conclude that probe **A** is suitable for monitoring intracellular pH without interference from other biologically relevant reactive species.

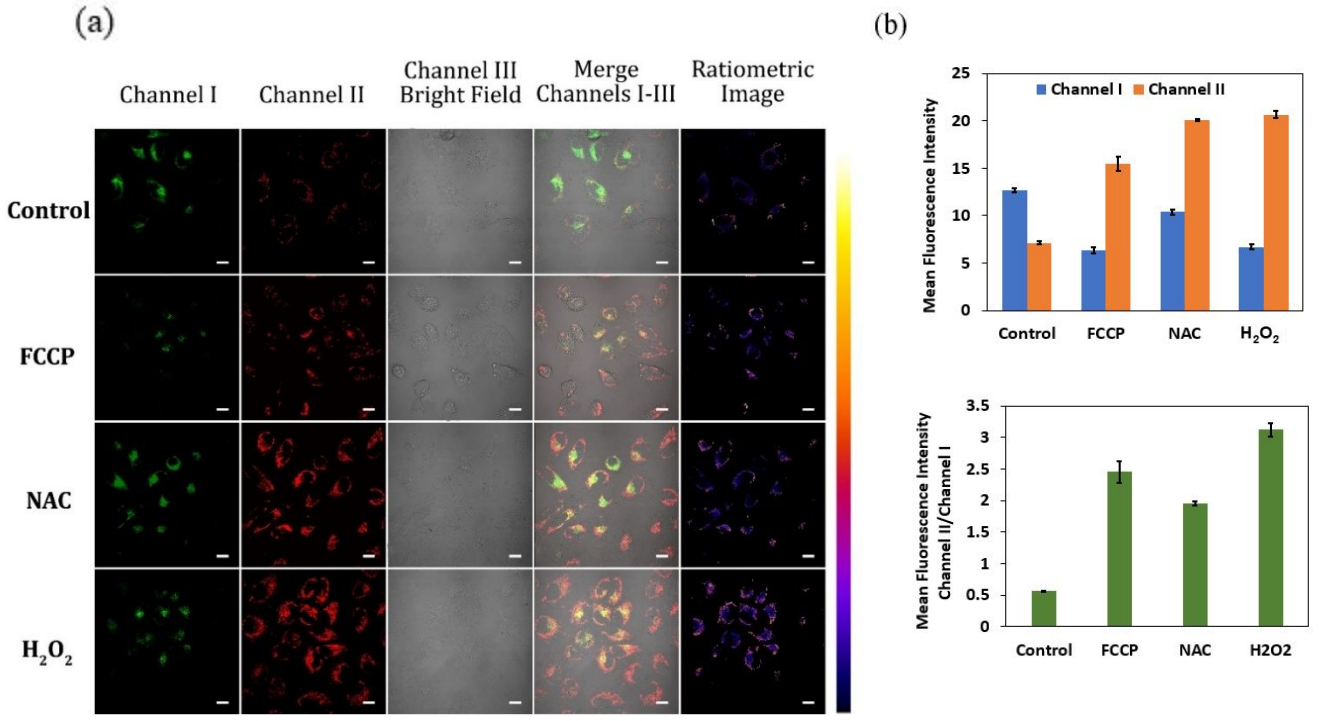

Figure 7. (a) Fluorescence images of HeLa cells were captured following 20 minutes of treatment with FCCP (10 μM), NAC (1 mM), or H_2O_2 (500 μM) while incubated with 10 μM of probe **A** in standard culture medium. The green channel (Channel I) was employed to detect visible fluorescence from probe **A** in the emission range of 425–525 nm, while the red channel (Channel II) was used to capture near-infrared fluorescence between 600–675 nm. Green fluorescence was visualized using Alexa Fluor 405 (excitation at 405 nm), and red fluorescence was monitored using Alexa Fluor 568 (excitation at 559 nm). All images are presented with a scale bar of 50 μm. (b) The histograms illustrate the emission intensities of Channel I (green) and Channel II (red) (top), and the fluorescence intensity ratio of Channel II to Channel I for probe **A** in HeLa cells (bottom) treated with the different chemicals, as quantified from the corresponding fluorescence images with SD bars based on n=3.

The cytotoxicity of probe **A** on HeLa cells was assessed using an MTT assay[59], as shown in Fig. 8. HeLa cells were incubated with varying concentrations of probe **A** for 24 hours. Even at high concentrations of 20 μM and 25 μM, cell viabilities of 90.3% and 81.2%, respectively, were observed. These results demonstrate that probe **A** exhibits low cytotoxicity, highlighting its potential as a safe fluorescent probe for monitoring dynamic biological processes in live cells.

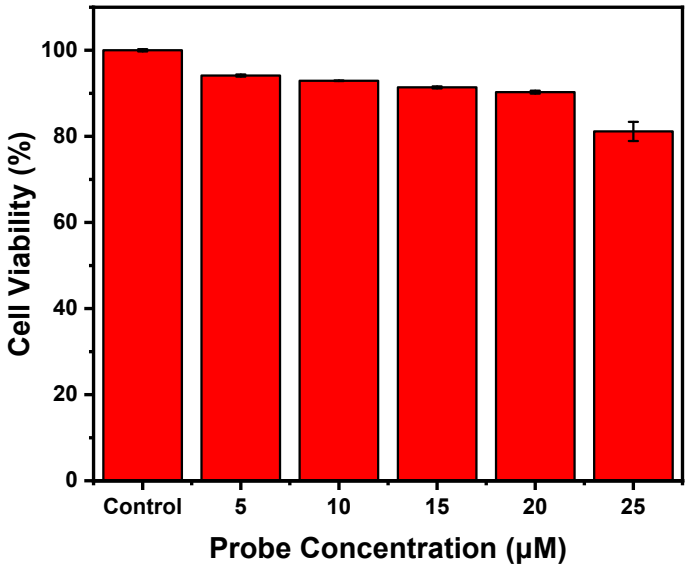

Figure 8. Assessment of cytotoxicity and cell proliferation using an MTT assay for probe **A.** HeLa cells were exposed to probe **A** at concentrations of 5, 10, 15, 20, and 25 μM for 24 hours. Cell viability was subsequently evaluated by introducing an MTT reagent (0.5 mg/mL) and measuring absorbance at 570 nm. The cell viability, directly proportional to the absorbance at 570 nm, was normalized against control cells (untreated with probe **A**). Error bars represent the mean ± standard deviation based on three independent measurements.

Due to their nearly transparent body, small size, short generation time, and ease of cultivation, *Drosophila melanogaster* first-instar larvae are widely used as models for *in vivo* imaging.[60] In this study, first-instar larvae were incubated with probe **A** (10 μM) in five different buffer solutions for 6 hours. In a basic environment (pH 9.0), the larvae exhibited strong fluorescence in the green channel (Channel I) but very weak fluorescence in the red channel (Channel II), resulting in a yellowish-green appearance in the merged fluorescence image, as shown in Fig. 9(a). With increasing H^+ ion concentrations, a gradual increase in red-channel fluorescence and a corresponding decrease in green-channel fluorescence were observed. In an acidic environment (pH 3.3), the larvae displayed intense fluorescence in the red channel and weak fluorescence in the green channel, producing a yellowish-red appearance in the merged image. Fig. 9(b) illustrates the percentage increase in intensity of Channel II and the percentage decrease in intensity of Channel I with increasing pH values. These results demonstrate that the ratiometric fluorescence response of probe **A** to pH functions effectively in a physiological environment, making it a suitable tool for monitoring pH fluctuations in various biological and pathological processes.

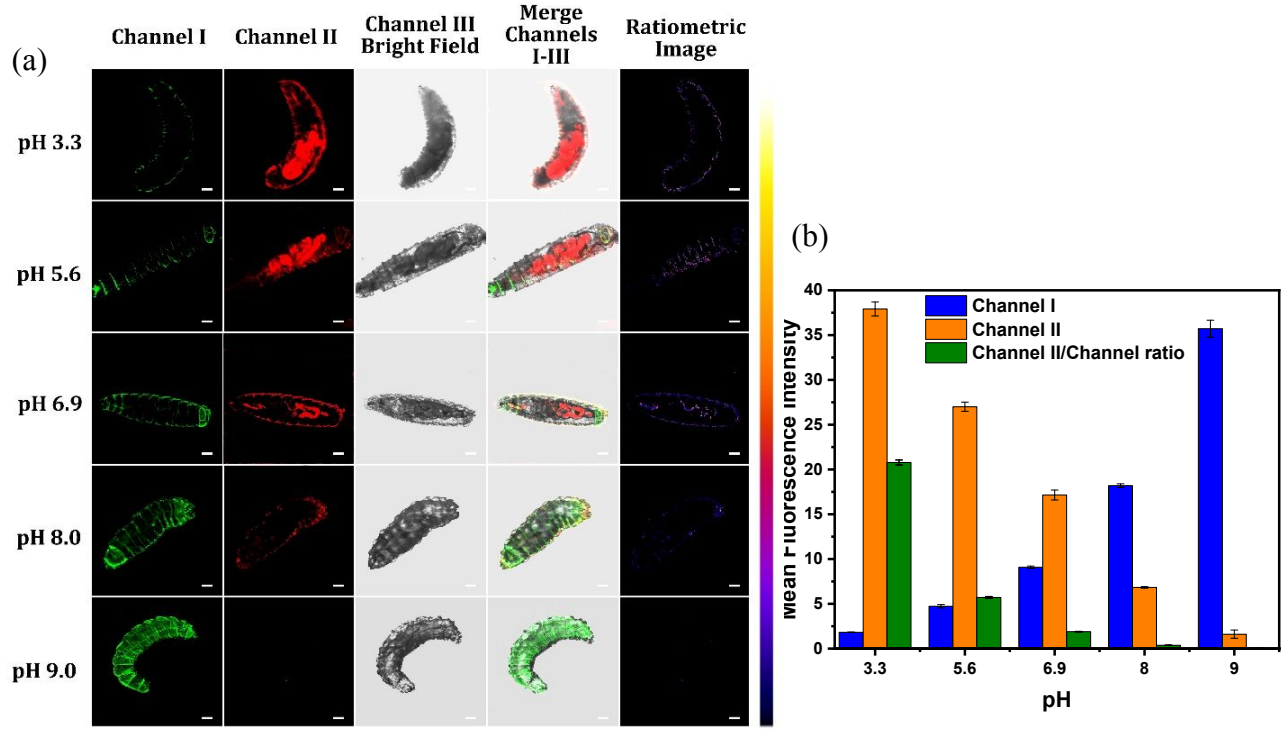

Figure 9. (a) Fluorescence images of *Drosophila melanogaster* first-instar larvae treated with 10 μM probe **A** in buffers of varying pH were captured. The green channel (Channel I) was used to visualize the probe's fluorescence within the emission range of 425–525 nm, while the red channel (Channel II) detected near-infrared fluorescence from 600–700 nm. Green fluorescence was observed using Alexa Fluor 405 (excitation at 405 nm), and red fluorescence was monitored using Alexa Fluor 568 (excitation at 559 nm). All images are presented with a scale bar of 50 μm. (b) The histogram displays the emission intensities of Channel I (green) and Channel II (red) for probe **A** in *D. melanogaster* first-instar larvae at different pH levels, as quantified from the fluorescence images. The error bars are based on experiments conducted three times.

Fig. 10 illustrates a plot of the intensity ratio (i.e., channel II 600–700 nm/channel I 425–525 nm) versus pH, revealing a significant deviation in the data for HeLa cells and fruit fly larvae at low pH, whereas values at pH > 7 show closer correlation. This discrepancy may be attributable to viscosity effects. Interestingly, no significant changes in the ratiometric intensities were observed at pH 8.29, Fig. 10 (b), whereas a marked increase in ratiometric intensity was observed at pH 3.5, Fig. 10 (c) with increasing glycerol concentration. There is also a correlation (Pearson's r = 0.94) with the fluorescence intensity ratios (654/465 nm) and glycerol concentration as shown in Fig. S44. These findings suggest that for the probe to function as an effective pH sensor within HeLa cells and fruit fly larvae, it is essential to generate cell-specific ratiometric intensity plots versus pH, using healthy cells and larvae. This would allow for the establishment of a similar correlation to that observed for ratiometric intensities in buffers of varying pH, as shown in Fig. 10(a). Furthermore, the probe has the potential to monitor viscosity changes in cells at low pH. Notably, the viscosity-dependent effect of probe **A** at low pH, resulting in $\mathbf{AH}^+$, Scheme 3, arises from ring opening, which induces a more flexible molecular structure. The fluorescence response mechanism is governed by the viscosity-dependent inhibition of molecular rotor rotation. In low-viscosity environments, free rotation facilitates the formation of a twisted intramolecular charge

transfer (TICT) state, leading to weak fluorescence. In contrast, higher viscosity restricts rotor rotation, thereby suppressing TICT and enhancing fluorescence intensity.[61–63]

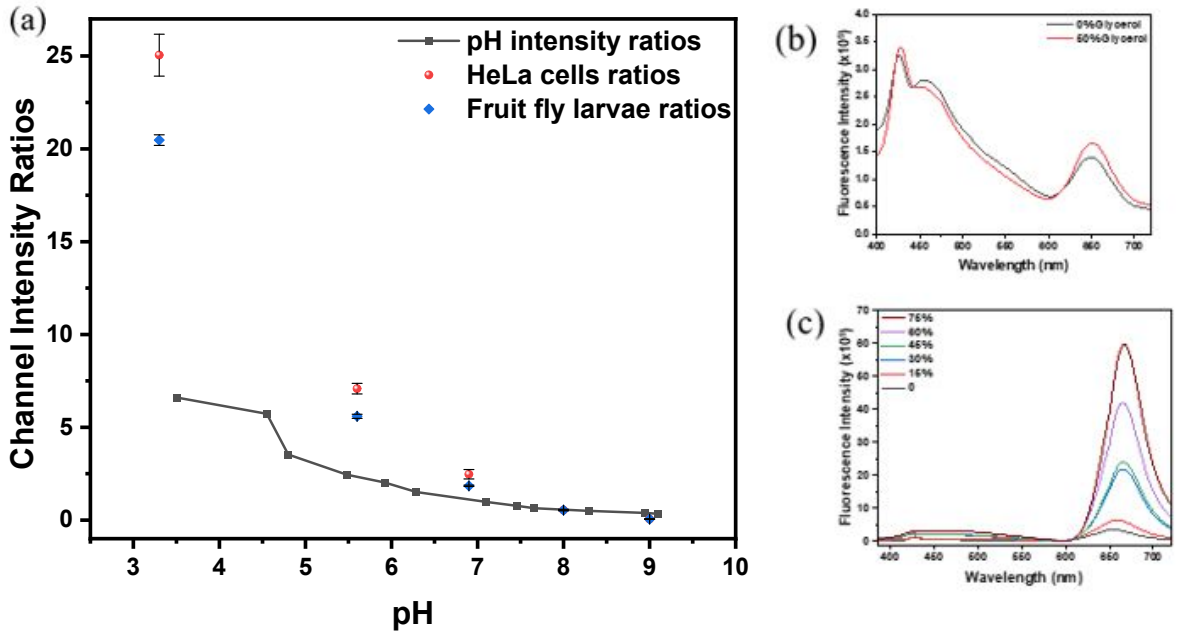

Figure 10. (a) Fluorescence intensity ratios of red (650 nm) to green 560 nm) channels from pH-dependent optical fluorescence measurements in solution (fluorometer), HeLa cells, and *Drosophila melanogaster* first-instar larvae treated with 10 μm probe **A** in buffers of varying pH. (b) Fluorescence spectra of probe **A** in buffer (pH 8.29) and in a 50% glycerol mixture. (c) Fluorescence spectra of probe $\mathbf{AH}^+$ in buffer (pH 3.50) with varying concentrations of glycerol. Error bars based on n = 3 determinations.

In order to explore the applicability of probe **A** to monitor viscosity, the effect of different concentrations of nystatin on HeLa cells was examined, Fig. 11. Nystatin binds to ergosterol on the cell membrane creating pores resulting in increased permeability. This has been shown to increase intracellular viscosity and molecular crowding.[64] We decided to conduct these experiments at a pH of 3.8 to see if with "healthy" HeLa cells the channel intensity ratio would fall on the line connecting the polynomial fitted points in Fig. 10 for the HeLa cell data. As can be seen in Fig. 12, the data for the control is situated on the line from the pH data in Fig. 10 suggesting that these would be the data to employ if one was measuring the pH levels in "healthy" HeLa cells. As can be seen in Figs. 11 and 12, changes in viscosity can also be monitored with probe **A** as there is an increase in the channel ratio with a corresponding increase in nystatin. Unfortunately, at concentrations greater than 30 mM of nystatin, the cells were not viable and died. These experiments suggest that to employ probe **A** to measure pH, the polynomial plot using the data in Fig. 10 for the HeLa cells and fruit fly larvae could be used for pH values greater than 7. However, if the ratio of the channel intensities is higher than the respective polynomial plots, then another probe should be utilized to independently verify the pH level since there may be viscosity issues.

These results suggest that changes in fluxionality in a molecular probe as the pH varies may influence emission intensity due to its response to viscosity.

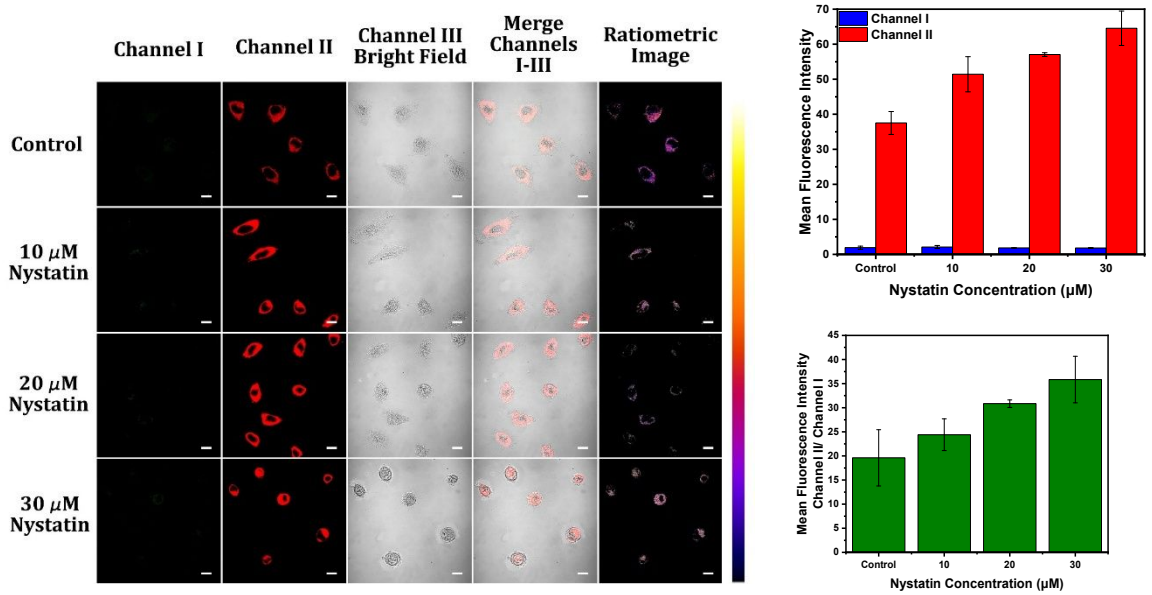

Figure 11. Fluorescence images of HeLa cells were captured following 320 minutes of treatment with different concentrations of nystatin (10, 20, and 30 μM) at pH 3.8. Green fluorescence was visualized using Alexa Fluor 405 (excitation at 405 nm), and red fluorescence was monitored using Alexa Fluor 568 (excitation at 559 nm). All images are presented with a scale bar of 50 μm. The histograms illustrate the emission intensities of Channel I (blue), and Channel II (red) (top), and the fluorescence intensity ratio of Channel II to Channel I (green) for probe **A** in HeLa cells (bottom), as quantified from the corresponding fluorescence images with SD bars based on n=3.

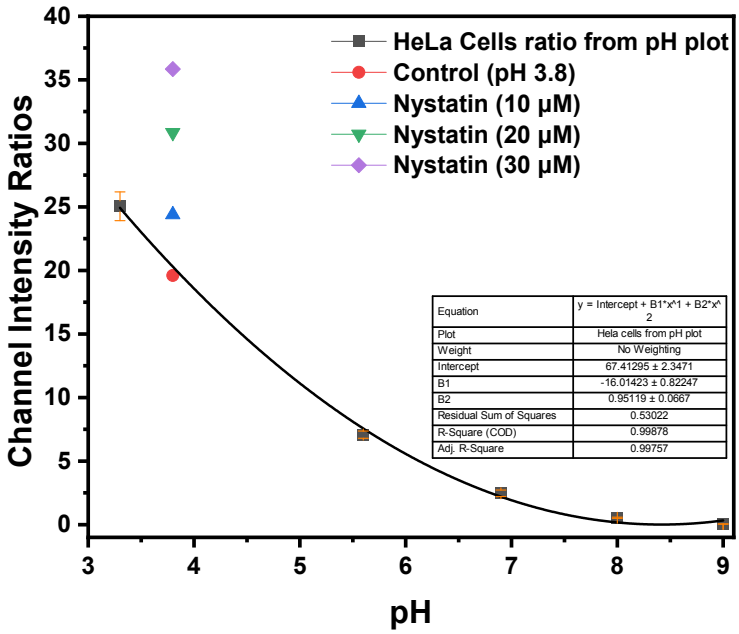

Figure 12. The pH versus channel intensity ratios were fitted using polynomial fitting. The channel intensity ratios for the control at pH 3.8 are found on the polynomial fitted line of the pH plot obtained using the data for the HeLa cells in Fig. 10.

Conclusion

In this study, we developed two fluorescent probes through straightforward synthetic protocols: Probe **A**, created by coupling a rhodamine moiety with a 7-nitrobenzofurazan group, and probe **B**, synthesized by linking a rhodamine moiety with a 7-(diethylamino)-2-oxo-3,8a-dihydro-2H-chromene-3-carbaldehyde group. Optical measurements revealed ratiometric emission profiles with pKa values of 4.430 for probe **A** and 4.144 for probe **B**, making them suitable for intracellular pH detection in living cells. Probe **A** demonstrated reversible ratiometric fluorescence responses to pH changes, enabling the monitoring of mitochondrial acidification in live HeLa cells treated with FCCP, NAC, H_2O_2, under hypoxia, or during mitophagy induced by nutrient deprivation. Furthermore, probe **A** was successfully employed to track pH changes in Drosophila melanogaster first-instar larvae using ratiometric emission intensities under two excitation channels. This study highlights the utility of a nontoxic, mitochondria-targeting probe **A** for selective pH monitoring through ratiometric fluorescence in living systems, offering a valuable tool for studying dynamic biological and pathological processes. An examination of the data obtained by looking at a graph of channel intensity ratios vs pH indicated deviations with the data for HeLa cells and fruit fly larvae. These were demonstrated to be viscosity-induced and confirmed by tests with nystatin. These results showed that the probe exhibited dual-probe capabilities and could be used to assess pH levels accurately at pH > 7, but for lower pH, the probe could qualitatively assess viscosity, if the pH was verified using another probe.

Supporting Information

Syntheses and characterizations of fluorescent probes, evaluations of their photostability and cytotoxicity, and their applications in live-cell imaging and pH monitoring. Detailed NMR, LC-MS, and fluorescence analyses, including pH-dependent fluorescence response, stability, and selectivity against ions and amino acids. Confocal imaging for lysosome localization and fluorescence spectra in varying glycerol concentrations. Results of theoretical calculations including xyz coordinates, vibrational spectra, UV-Vis spectra, and molecular orbital representations.

Conflicts of interest

The authors state that there are no financial conflicts of interest.

Author Information

Corresponding Author

Rudy L. Luck, Department of Chemistry, Michigan Technological University, Houghton, Michigan 49931, United States; Orcid: https://orcid.org/0000-0001-5436-1942; Email: rluck@mtu.edu

Acknowledgments

This work was based on support received from the National Institute of General Medical Sciences, National Institutes of Health, through Award Number R15GM152969-01 to R. L. Luck and H. Liu. The study was also assisted with partial sponsorship from the National Institute of General Medical Sciences, National Institutes of Health, through Award Number R15 GM146206-01 for H. Liu and R. L Luck. The authors also extend their appreciation to the National Science Foundation for their financial support under award number 2117318 for the acquisition of a new NMR spectrometer. Computational calculations for fluorescent probes were performed utilizing a high-performance computing infrastructure based at Michigan Technological University.

References

(1) Casey, J. R.; Grinstein, S.; Orlowski, J. Sensors and Regulators of Intracellular pH. *Nat. Rev. Mol. Cell Biol.* **2010**, *11* (1), 50–61. https://doi.org/10.1038/nrm2820.

(2) Appelqvist, H.; Wäster, P.; Kågedal, K.; Öllinger, K. The Lysosome: From Waste Bag to Potential Therapeutic Target. *J. Mol. Cell Biol.* **2013**, *5* (4), 214–226. https://doi.org/10.1093/jmcb/mjt022.

(3) Orij, R.; Urbanus, M. L.; Vizeacoumar, F. J.; Giaever, G.; Boone, C.; Nislow, C.; Brul, S.; Smits, G. J. Genome-Wide Analysis of Intracellular pH Reveals Quantitative Control of Cell Division Rate by pHc in Saccharomyces Cerevisiae. *Genome Biol.* **2012**, *13* (9), R80. https://doi.org/10.1186/gb-2012-13-9-r80.

(4) Lagadic-Gossmann, D.; Huc, L.; Lecureur, V. Alterations of Intracellular pH Homeostasis in Apoptosis: Origins and Roles. *Cell Death Differ.* **2004**, *11* (9), 953–961. https://doi.org/10.1038/sj.cdd.4401466.

(5) Orij, R.; Brul, S.; Smits, G. J. Intracellular pH Is a Tightly Controlled Signal in Yeast. *Biochim. Biophys. Acta BBA - Gen. Subj.* **2011**, *1810* (10), 933–944. https://doi.org/10.1016/j.bbagen.2011.03.011.

(6) Putnam, R. W. 22 - Intracellular pH Regulation. In *Cell Physiology Source Book (Third Edition)*; Sperelakis, N., Ed.; Academic Press: San Diego, **2001**; pp 357–372. https://doi.org/10.1016/B978-012656976-6/50114-1.
(7) Martin, C.; Pedersen, S. F.; Schwab, A.; Stock, C. Intracellular pH Gradients in Migrating Cells. *Am. J. Physiol.-Cell Physiol.* **2011**, *300* (3), C490–C495. https://doi.org/10.1152/ajpcell.00280.2010.
(8) Liu, M.; Lv, Y.; Jie, X.; Meng, Z.; Wang, X.; Huang, J.; Peng, A.; Tian, Z. A Super-Sensitive Ratiometric Fluorescent Probe for Monitoring Intracellular Subtle pH Fluctuation. *Sens. Actuators B Chem.* **2018**, *273*, 167–175. https://doi.org/10.1016/j.snb.2018.06.048.
(9) Dwivedi, S. K.; Arachchige, D. L.; Olowolagba, A. M.; Mahmoud, M.; Pandey, S.; Vohs, T.; Liu, H.; Luck, R. L. Near-Infrared Ratiometric Hemicyanine Fluorescent Probes for Monitoring Mitochondrial pH Dynamics in Live Cells during Oxidative Stress and Hypoxia. *ACS Omega* **2024**, *9* (40), 42049–42060. https://doi.org/10.1021/acsomega.4c07303.
(10) Matsuyama, S.; Reed, J. C. Mitochondria-Dependent Apoptosis and Cellular pH Regulation. *Cell Death Differ.* **2000**, *7* (12), 1155–1165. https://doi.org/10.1038/sj.cdd.4400779.
(11) Abad, M. F. C.; Benedetto, G. D.; Magalhães, P. J.; Filippin, L.; Pozzan, T. Mitochondrial pH Monitored by a New Engineered Green Fluorescent Protein Mutant*. *J. Biol. Chem.* **2004**, *279* (12), 11521–11529. https://doi.org/10.1074/jbc.M306766200.
(12) Gincel, D.; Zaid, H.; Shoshan-Barmatz, V. Calcium Binding and Translocation by the Voltage-Dependent Anion Channel: A Possible Regulatory Mechanism in Mitochondrial Function. *Biochem. J.* **2001**, *358* (1), 147–155. https://doi.org/10.1042/bj3580147.
(13) Hajnóczky, G.; Csordás, G.; Yi, M. Old Players in a New Role: Mitochondria-Associated Membranes, VDAC, and Ryanodine Receptors as Contributors to Calcium Signal Propagation from Endoplasmic Reticulum to the Mitochondria. *Cell Calcium* **2002**, *32* (5), 363–377. https://doi.org/10.1016/S0143416002001872.
(14) Ernster, L.; Schatz, G. Mitochondria: A Historical Review. *J. Cell Biol.* **1981**, *91* (3), 227s–255s. https://doi.org/10.1083/jcb.91.3.227s.
(15) Li, X.; Fang, P.; Mai, J.; Choi, E. T.; Wang, H.; Yang, X. Targeting Mitochondrial Reactive Oxygen Species as Novel Therapy for Inflammatory Diseases and Cancers. *J. Hematol. Oncol.* **2013**, *6* (1), 19. https://doi.org/10.1186/1756-8722-6-19.
(16) Niu, L.-Q.; Huang, J.; Yan, Z.-J.; Men, Y.-H.; Luo, Y.; Zhou, X.-M.; Wang, J.-M.; Wang, J.-H. Fluorescence Detection of Intracellular pH Changes in the Mitochondria-Associated Process of Mitophagy Using a Hemicyanine-Based Fluorescent Probe. *Spectrochim. Acta. A. Mol. Biomol. Spectrosc.* **2019**, *207*, 123–131. https://doi.org/10.1016/j.saa.2018.09.015.
(17) Shu, W.; Yu, J.; Li, Z.; Sun, X.; Wang, Y.; Wu, Y.; Qin, J.; Zhang, Y.; Xiao, H.; Zhang, X. A Mitochondrial Suitable Ratiometric Fluorescent Probe for Tracking pH Change during Mitophagy. *Sens. Actuators B Chem.* **2022**, *369*, 132323. https://doi.org/10.1016/j.snb.2022.132323.
(18) Wang, H.; Hu, J.; Yang, G.; Zhang, X.; Zhang, R.; Uvdal, K.; Zhang, Z.; Wu, X.; Hu, Z. Real-Time Tracking of Mitochondrial Dynamics by a Dual-Sensitive Probe. *Sens. Actuators B Chem.* **2020**, *320*, 128418. https://doi.org/10.1016/j.snb.2020.128418.
(19) Maulucci, G.; Chiarpotto, M.; Papi, M.; Samengo, D.; Pani, G.; De Spirito, M. Quantitative Analysis of Autophagic Flux by Confocal pH-Imaging of Autophagic Intermediates. *Autophagy* **2015**, *11* (10), 1905–1916. https://doi.org/10.1080/15548627.2015.1084455.
(20) Lee, M. H.; Park, N.; Yi, C.; Han, J. H.; Hong, J. H.; Kim, K. P.; Kang, D. H.; Sessler, J. L.; Kang, C.; Kim, J. S. Mitochondria-Immobilized pH-Sensitive Off–On Fluorescent Probe. *J. Am. Chem. Soc.* **2014**, *136* (40), 14136–14142. https://doi.org/10.1021/ja506301n.
(21) Song, Y.; Zheng, Y.; Zhang, S.; Song, Y.; Niu, M.; Li, Y.; Ye, Z.; Yu, H.; Zhang, M.; Xiao, Y. Always-on and Water-Soluble Rhodamine Amide Designed by Positive Charge Effect and Application in Mitochondrion-Targetable Imaging of Living Cells. *Sens. Actuators B Chem.* **2019**, *286*, 32–38. https://doi.org/10.1016/j.snb.2019.01.107.

(22) Wang, T.-R.; Chen, Q.; Tang, M.-Y.; Zhang, Y.; Shen, S.-L.; Cao, X.-Q. Visual Monitoring of the Mitochondrial pH Changes during Mitophagy with a NIR Fluorescent Probe and Its Application in Tumor Imaging. *Spectrochim. Acta. A. Mol. Biomol. Spectrosc.* **2022**, *280*, 121496. https://doi.org/10.1016/j.saa.2022.121496.
(23) Liu, X.; Wang, L.; Bing, T.; Zhang, N.; Dihua Shangguan. A Mitochondria-Targeted Ratiometric Fluorescent pH Probe. *ACS Appl. Bio Mater.* **2019**, *2* (3), 1368–1375. https://doi.org/10.1021/acsabm.9b00061.
(24) Feng, Z.; Wu, J.; Jiang, M.; Sha, J.; Liu, W.; Ren, H.; Zhang, W.; Lee, C.-S.; Wang, P. A Rhodamine Derivative-Based Fluorescent Probe for Visual Monitoring of pH Changes in the Golgi Apparatus. *Sens. Actuators B Chem.* **2022**, *366*, 131963. https://doi.org/10.1016/j.snb.2022.131963.
(25) Bai, Q.; Yang, C.; Yang, M.; Pei, Z.; Zhou, X.; Liu, J.; Ji, H.; Li, G.; Wu, M.; Qin, Y.; Wang, Q.; Wu, L. pH-Dominated Selective Imaging of Lipid Droplets and Mitochondria via a Polarity-Reversible Ratiometric Fluorescent Probe. *Anal. Chem.* **2022**, *94* (6), 2901–2911. https://doi.org/10.1021/acs.analchem.1c04806.
(26) Mao, G.-J.; Zhang, S.-Y.; Yang, T.-T.; Zhu, B.; Sun, X.-Y.; Wang, Q.-Q.; Zhang, G. A Tumor-Targeting Two-Photon Fluorescent Probe with a Far-Red to NIR Emission for Imaging Basal Hypochlorite in Cancer Cells and Tumor. *Talanta* **2024**, *277*, 126436. https://doi.org/10.1016/j.talanta.2024.126436.
(27) Na Kim, H.; Hee Lee, M.; Jung Kim, H.; Seung Kim, J.; Yoon, J. A New Trend in Rhodamine-Based Chemosensors: Application of Spirolactam Ring-Opening to Sensing Ions. *Chem. Soc. Rev.* **2008**, *37* (8), 1465–1472. https://doi.org/10.1039/B802497A.
(28) Lee, D.; Swamy, K. M. K.; Hong, J.; Lee, S.; Yoon, J. A Rhodamine-Based Fluorescent Probe for the Detection of Lysosomal pH Changes in Living Cells. *Sens. Actuators B Chem.* **2018**, *266*, 416–421. https://doi.org/10.1016/j.snb.2018.03.133.
(29) Niu, G.; Zhang, P.; Liu, W.; Wang, M.; Zhang, H.; Wu, J.; Zhang, L.; Wang, P. Near-Infrared Probe Based on Rhodamine Derivative for Highly Sensitive and Selective Lysosomal pH Tracking. *Anal. Chem.* **2017**, *89* (3), 1922–1929. https://doi.org/10.1021/acs.analchem.6b04417.
(30) Zhu, N.; Xu, J.; Ma, Q.; Geng, Y.; Li, L.; Liu, S.; Liu, S.; Wang, G. Rhodamine-Based Fluorescent Probe for Highly Selective Determination of Hg^{2+}. *ACS Omega* **2022**, *7* (33), 29236–29245. https://doi.org/10.1021/acsomega.2c03336.
(31) Yang, L.-L.; Zou, S.-Y.; Fu, Y.-H.; Li, W.; Wen, X.-P.; Wang, P.-Y.; Wang, Z.-C.; Ouyang, G.-P.; Li, Z.; Yang, S. Highly Selective and Sensitive Detection of Biogenic Defense Phytohormone Salicylic Acid in Living Cells and Plants Using a Novel and Viable Rhodamine-Functionalized Fluorescent Probe. *J. Agric. Food Chem.* **2020**, *68* (15), 4285–4291. https://doi.org/10.1021/acs.jafc.9b06771.
(32) Vegesna, G. K.; Janjanam, J.; Bi, J.; Luo, F.-T.; Zhang, J.; Olds, C.; Tiwari, A.; Liu, H. pH-Activatable near-Infrared Fluorescent Probes for Detection of Lysosomal pH inside Living Cells. *J Mater Chem B* **2014**, *2* (28), 4500–4508. https://doi.org/10.1039/C4TB00475B.
(33) Zhou, X.; Su, F.; Lu, H.; Senechal-Willis, P.; Tian, Y.; Johnson, R. H.; Meldrum, D. R. An FRET-Based Ratiometric Chemosensor for *in Vitro* Cellular Fluorescence Analyses of pH. *Biomaterials* **2012**, *33* (1), 171–180. https://doi.org/10.1016/j.biomaterials.2011.09.053.
(34) Maity, D.; Karthigeyan, D.; Kundu, T. K.; Govindaraju, T. FRET-Based Rational Strategy for Ratiometric Detection of Cu2+ and Live Cell Imaging. *Sens. Actuators B Chem.* **2013**, *176*, 831–837. https://doi.org/10.1016/j.snb.2012.09.071.
(35) Zhang, Y.; Xia, S.; Wan, S.; Steenwinkel, T. E.; Vohs, T.; Luck, R. L.; Werner, T.; Liu, H. Ratiometric Detection of Glutathione Based on Disulfide Linkage Rupture between a FRET Coumarin Donor and a Rhodamine Acceptor. *ChemBioChem* **2021**, *22* (13), 2282–2291. https://doi.org/10.1002/cbic.202100108.
(36) Gryczynski, Z.; Gryczynski, I.; Lakowicz, J. R. [2] Fluorescence-Sensing Methods. In *Methods in Enzymology*; Biophotonics, Part A; Academic Press, **2003**; Vol. 360, pp 44–75. https://doi.org/10.1016/S0076-6879(03)60106-0.

(37) Austin, A.; Petersson, G. A.; Frisch, M. J.; Dobek, F. J.; Scalmani, G.; Throssell, K. A Density Functional with Spherical Atom Dispersion Terms. *J. Chem. Theory Comput.* **2012**, *8*, 4989–5007. https://doi.org/10.1021/ct300778e.
(38) Frisch, M. J.; Trucks, G. W.; Schlegel, H. B.; Scuseria, G. E.; Robb, M. A.; Cheeseman, J. R.; Scalmani, G.; Barone, V.; Petersson, G. A.; Nakatsuji, H.; Li, X.; Caricato, M.; Marenich, A. V.; Bloino, J.; Janesko, B. G.; Gomperts, R.; Mennucci, B.; Hratchian, H. P.; Ortiz, J. V.; Izmaylov, A. F.; Sonnenberg, J. L.; Williams-Young, D.; Ding, F.; Lipparini, F.; Egidi, F.; Goings, J.; Peng, B.; Petrone, A.; Henderson, T.; Ranasinghe, D.; Zakrzewski, V. G.; Gao, J.; Rega, N.; Zheng, G.; Liang, W.; Hada, M.; Ehara, M.; Toyota, K.; Fukuda, R.; Hasegawa, J.; Ishida, M.; Nakajima, T.; Honda, Y.; Kitao, O.; Nakai, H.; Vreven, T.; Throssell, K.; Montgomery, J., J. A.; Peralta, J. E.; Ogliaro, F.; Bearpark, M. J.; Heyd, J. J.; Brothers, E. N.; Kudin, K. N.; Staroverov, V. N.; Keith, T. A.; Kobayashi, R.; Normand, J.; Raghavachari, K.; Rendell, A. P.; Burant, J. C.; Iyengar, S. S.; Tomasi, J.; Cossi, M.; Millam, J. M.; Klene, M.; Adamo, C.; Cammi, R.; Ochterski, J. W.; Martin, R. L.; Morokuma, K.; Farkas, O.; Foresman, J. B.; Fox, D. J. Gaussian 16, Revision A.03, **2016**.
(39) Runge, E.; Gross, E. K. U. Density-Functional Theory for Time-Dependent Systems. *Phys. Rev. Lett.* **1984**, *52*, 997–1000. https://doi.org/10.1103/PhysRevLett.52.997.
(40) Tomasi, J.; Mennucci, B.; Cammi, R. Quantum Mechanical Continuum Solvation Models. *Chem. Rev.* **2005**, *105*, 2999–3094. https://doi.org/10.1021/cr9904009.
(41) Dennington, R.; Keith, T. A.; Millam, J. M. GaussView, Version 6.0.16, **2016**. http://gaussian.com/g_prod/gv5.htm.
(42) Macrae, C. F.; Bruno, I. J.; Chisholm, J. A.; Edgington, P. R.; McCabe, P.; Pidcock, E.; Rodriguez-Monge, L.; Taylor, R.; van de Streek, J.; Wood, P. A. Mercury CSD 2.0 - New Features for the Visualization and Investigation of Crystal Structures. *J. Appl. Crystallogr.*, **2008**, *41*, 466–470.
(43) Adamo, C.; Jacquemin, D. The Calculations of Excited-State Properties with Time-Dependent Density Functional Theory. *Chem. Soc. Rev.* **2013**, *42*, 845–856. https://doi.org/10.1039/C2CS35394F.
(44) Tauc, J.; Grigorovici, R.; Vancu, A. Optical Properties and Electronic Structure of Amorphous Germanium. *Phys. Status Solidi B* **1966**, *15* (2), 627–637. https://doi.org/10.1002/pssb.19660150224.
(45) Zhang, H.; Liu, J.; Sun, Y.-Q.; Liu, M.; Guo, W. Carbon–Dipyrromethenes: Bright Cationic Fluorescent Dyes and Potential Application in Revealing Cellular Trafficking of Mitochondrial Glutathione Conjugates. *J. Am. Chem. Soc.* **2020**, *142* (40), 17069–17078. https://doi.org/10.1021/jacs.0c06916.
(46) K. Vegesna, G.; Janjanam, J.; Bi, J.; Luo, F.-T.; Zhang, J.; Olds, C.; Tiwari, A.; Liu, H. pH-Activatable near-Infrared Fluorescent Probes for Detection of Lysosomal pH inside Living Cells. *J. Mater. Chem. B* **2014**, *2* (28), 4500–4508. https://doi.org/10.1039/C4TB00475B.
(47) Villa-Cuesta, E.; Holmbeck, M. A.; Rand, D. M. Rapamycin Increases Mitochondrial Efficiency by mtDNA-Dependent Reprogramming of Mitochondrial Metabolism in Drosophila. *J. Cell Sci.* **2014**, *127* (10), 2282–2290. https://doi.org/10.1242/jcs.142026.
(48) Sharma, M. Chapter 18 - Transdermal and Intravenous Nano Drug Delivery Systems: Present and Future. In *Applications of Targeted Nano Drugs and Delivery Systems*; Mohapatra, S. S., Ranjan, S., Dasgupta, N., Mishra, R. K., Thomas, S., Eds.; Micro and Nano Technologies; Elsevier, **2019**; pp 499–550. https://doi.org/10.1016/B978-0-12-814029-1.00018-1.
(49) D'Arcy, M. S. Mitophagy in Health and Disease. Molecular Mechanisms, Regulatory Pathways, and Therapeutic Implications. *Apoptosis* **2024**, *29* (9), 1415–1428. https://doi.org/10.1007/s10495-024-01977-y.
(50) Mao, Y.; Zhang, J.; Zhou, Q.; He, X.; Zheng, Z.; Wei, Y.; Zhou, K.; Lin, Y.; Yu, H.; Zhang, H.; Zhou, Y.; Lin, P.; Wu, B.; Yuan, Y.; Zhao, J.; Xu, W.; Zhao, S. Hypoxia Induces Mitochondrial Protein Lactylation to Limit Oxidative Phosphorylation. *Cell Res.* **2024**, *34* (1), 13–30. https://doi.org/10.1038/s41422-023-00864-6.

(51) Chen, P.-S.; Chiu, W.-T.; Hsu, P.-L.; Lin, S.-C.; Peng, I.-C.; Wang, C.-Y.; Tsai, S.-J. Pathophysiological Implications of Hypoxia in Human Diseases. *J. Biomed. Sci.* **2020**, *27* (1), 63. https://doi.org/10.1186/s12929-020-00658-7.

(52) Muz, B.; de la Puente, P.; Azab, F.; Azab, A. K. The Role of Hypoxia in Cancer Progression, Angiogenesis, Metastasis, and Resistance to Therapy. *Hypoxia* **2015**, *3*, 83–92. https://doi.org/10.2147/HP.S93413.

(53) Wagatsuma, A.; Arakawa, M.; Matsumoto, H.; Matsuda, R.; Hoshino, T.; Mabuchi, K. Cobalt Chloride, a Chemical Hypoxia-Mimicking Agent, Suppresses Myoblast Differentiation by Downregulating Myogenin Expression. *Mol. Cell. Biochem.* **2020**, *470* (1), 199–214. https://doi.org/10.1007/s11010-020-03762-2.

(54) Inoue, Y.; Wada, Y.; Sato, M.; Sato, S.; Okamoto, T.; Kanemoto, N. Carbonyl Cyanide-4-(Trifluoromethoxy)Phenylhydrazone-Induced Toxicities in Rats: Comparative Study with Other Mitochondrial Uncouplers (2,4-Dinitrophenol, OPC-163493 and Tolcapone). *Toxicol. Res.* **2023**, *39* (4), 611–623. https://doi.org/10.1007/s43188-023-00189-x.

(55) Kumar, P.; Osahon, O. W.; Sekhar, R. V. GlyNAC (Glycine and N-Acetylcysteine) Supplementation in Mice Increases Length of Life by Correcting Glutathione Deficiency, Oxidative Stress, Mitochondrial Dysfunction, Abnormalities in Mitophagy and Nutrient Sensing, and Genomic Damage. *Nutr.* **2022**, *14* (5), 1114. https://doi.org/10.3390/nu14051114.

(56) Grayson, C.; Faerman, B.; Koufos, O.; Mailloux, R. J. Fatty Acid Oxidation Drives Mitochondrial Hydrogen Peroxide Production by α-Ketoglutarate Dehydrogenase. *J. Biol. Chem.* **2024**, *300* (4), 107159. https://doi.org/10.1016/j.jbc.2024.107159.

(57) Lenzen, S.; Lushchak, V. I.; Scholz, F. The Pro-Radical Hydrogen Peroxide as a Stable Hydroxyl Radical Distributor: Lessons from Pancreatic Beta Cells. *Arch. Toxicol.* **2022**, *96* (7), 1915–1920. https://doi.org/10.1007/s00204-022-03282-6.

(58) Juan, C. A.; Pérez de la Lastra, J. M.; Plou, F. J.; Pérez-Lebeña, E. The Chemistry of Reactive Oxygen Species (ROS) Revisited: Outlining Their Role in Biological Macromolecules (DNA, Lipids and Proteins) and Induced Pathologies. *Int. J. Mol. Sci.* **2021**, *22* (9), 4642. https://doi.org/10.3390/ijms22094642.

(59) Ghasemi, M.; Liang, S.; Luu, Q. M.; Kempson, I. The MTT Assay: A Method for Error Minimization and Interpretation in Measuring Cytotoxicity and Estimating Cell Viability. In *Cell Viability Assays: Methods and Protocols*; Friedrich, O., Gilbert, D. F., Eds.; Springer US: New York, NY, **2023**; pp 15–33. https://doi.org/10.1007/978-1-0716-3052-5_2.

(60) Demir, E.; Demir, F. T.; Marcos, R. Drosophila as a Suitable In Vivo Model in the Safety Assessment of Nanomaterials. In *Nanotoxicology in Safety Assessment of Nanomaterials*; Louro, H., Silva, M. J., Eds.; Springer International Publishing: Cham, **2022**; pp 275–301. https://doi.org/10.1007/978-3-030-88071-2_12.

(61) Fu, J.; He, S.; Liu, J.; Pang, J.; Wang, K.-N.; Chen, Y. A Novel High Signal-to-Noise Ratio Fluorescent Probe for Real-Time Mitochondrial Viscosity Detection and Imaging in Vitro and in Vivo. *J. Mater. Chem. B* **2024**, *12* (41), 10635–10643. https://doi.org/10.1039/d4tb01486c.

(62) Li, Y.-Y.; Hu, J.-L.; Wu, J.-R.; Wang, Y.-R.; Zhang, A.-H.; Tan, Y.-W.; Shang, Y.-J.; Liang, T.; Li, M.; Meng, Y.-L.; Kang, Y.-F. Multifunctional Fluorescence Probe for Simultaneous Detection of Viscosity, Polarity, and $ONOO^-$ and Its Bioimaging in Vitro and Vivo. *Biosens. Bioelectron.* **2024**, *254*, 116233. https://doi.org/10.1016/j.bios.2024.116233.

(63) Liu, F.-T.; Wang, S.; Wang, Y.-P.; Jiang, P.-F.; Miao, J.-Y.; Zhao, B.-X.; Lin, Z.-M. A Near-Infrared Fluorescent Probe Based FRET for Ratiometric Sensing of H_2O_2 and Viscosity in Live Cells. *Talanta* **2024**, *275*, 126135. https://doi.org/10.1016/j.talanta.2024.126135.

(64) Tang, F.; Wang, K.; Liu, X.; Zhang, X.; Zhou, W.; Mu, Z.; Zhang, T.; Shu, W.; Liu, Y.; Xiao, H. Small Molecular Fluorescent Probes for Alzheimer's Disease Associated Active Species. *Chem. – Eur. J.* **2023**, *29* (35), e202300592. https://doi.org/10.1002/chem.202300592.

Data Availability Statement

The datasets supporting the findings of this study are available within the article and its Electronic Supplementary Information (ESI). Additional raw data or analysis files are available from the corresponding author upon reasonable request.